Leveraging xGEO Orbits for Cislunar Space Domain Awareness

THESIS

Jay Laone, 2Lt, USAF

AFIT-ENY-MS-22-M-302

DEPARTMENT OF THE AIR FORCE
AIR UNIVERSITY

AIR FORCE INSTITUTE OF TECHNOLOGY

Wright-Patterson Air Force Base, Ohio

AFIT-ENY-MS-22-M-302

LEVERAGING XGEO ORBITS FOR CISLUNAR SPACE DOMAIN AWARENESS

THESIS

Presented to the Faculty

Department of Aeronautics and Astronautics

Graduate School of Engineering and Management

Air Force Institute of Technology

Air University

Air Education and Training Command

in Partial Fulfillment of the Requirements for the

Degree of Master of Science in Space Systems

Jay Laone, B.S.

2Lt, USAF

March 2022

AFIT-ENY-MS-22-M-302

LEVERAGING XGEO ORBITS FOR CISLUNAR SPACE DOMAIN AWARENESS

Jay Laone, B.S.
2Lt, USAF

Committee Membership:

Bryan Little, Lt Col
Chairman

Costantinos Zagaris, Maj
Member

David Meyer
Member

Abstract

With recent interest in using cislunar orbits for a variety of missions, it is more important than ever to also have cislunar space domain awareness (SDA), a mission currently performed by the United States Space Force. Some of the SDA architectures proposed in literature have discussed using cislunar orbits to perform SDA, but these orbits are difficult to track and maintain, adding uncertainty to the observer position. LEO/GEO architectures follow the two-body assumption and their orbits are easy to maintain, but provide limited capability against cislunar test targets. This thesis aims to bridge the gap between traditional LEO/GEO architectures and the new cislunar orbit architectures with orbits higher than GEO but still within the Earth sphere of influence, called xGEO. This research effort first explores the feasibility of xGEO orbits by examining the errors that the two-body assumption builds over time. Findings suggest that the two body assumption can be used to varying degrees depending on the orbit radius. This study has found that regardless of radius from 2-5xGEO, when the orbit is in the lunar plane, the majority of the error is in-track. The study then evaluates how well these orbits perform when observing a lunar mission test satellite. The observational simulations resulted in long observation times with high SNR, although the study only used a single plane and one sensor design for each simulation. Lastly, this study explores the possibility of using xGEO orbits for an inspection mission at L_1. Using a circular restricted three body (CR3BP) model, trajectories were successfully created from 2-5xGEO using the stable manifolds with minimal Δv and time of flight. Results show diminishing returns in both Δv and time of flight between 3 and 4xGEO.

Acknowledgements

I'd like to thank my parents for encouraging my interest in the sciences and supporting me during my academic journey. Without them, I wouldn't be the person I am today. I would also like to thank my thesis advisor Lt Col Little for all his advice and time spent throughout my thesis effort.

Jay Laone

Table of Contents

Page

List of Figures

List of Tables

List of Abbreviations

Abbreviation		Page
SDA	Space Domain Awareness	1
USSF	United States Space Force	1
SOI	Sphere of Influence	2
CR3BP	Circular Restricted Three Body Problem	3
CONOP	Concept of Operations	3
MUI	Modeled Universe of Interest	41

LEVERAGING XGEO ORBITS FOR CISLUNAR SPACE DOMAIN AWARENESS

I. Introduction

Until recently, only the region of space extending to GEO has been utilized, roughly a radius of 22,236 miles, such that only near-Earth space domain awareness (SDA) was necessary for the U.S. Air Force and now U.S. Space Force [1, 2]. However, with renewed interest in cislunar space by both private and public U.S. entities, it is a greater necessity than ever for the USSF to have persistent SDA in all of cislunar space, defined as 272,000 miles and beyond. This is a tenfold increase in range and a 10^3 increase in volume, and cannot be done by legacy SDA sensors in GEO alone [1]. This is due to the fact that GEO satellites regardless of constellation size will add little to no observational capability to this mission since they have limited geometric diversity. In addition, due to the large span of space cislunar orbits travel through, the observer to target distance can be very large.

In an attempt to alleviate the problem, there has been much discussion about missions that rely on orbits about the Lagrange points, equilibrium points that exist in the Earth-Moon system. They provide better geometric diversity and are closer in range to many objects of interest in cislunar space, and thus, when added to existing SDA sensors, give greatly increased SDA capability [3]. SDA also requires unobstructed lines of sight (pointing constraints) and adequate target illumination, which cislunar observation sensors may provide depending on the orbit. However, these cislunar-based architectures have the problem of being far away from Earth, as well as problems with stability and predictability, making reliable communication

with Earth difficult [3].

A way to bridge the gap between "traditional" near Earth and cislunar architectures are orbits beyond GEO but still dominated by Earth's two-body dynamics. As seen in Fig. 1, a way to explore possible orbits are using "spheres of influence", or SOI [2]. Anything within a system's SOI can be closely approximated just by using those bodies in the system. The dashed circles represent the three-dimensional spheres that divide different SOIs. The y axis labels the SOIs, while the x axis gives the measurements in terms of the GEO radius. For example, the Earth SOI (within

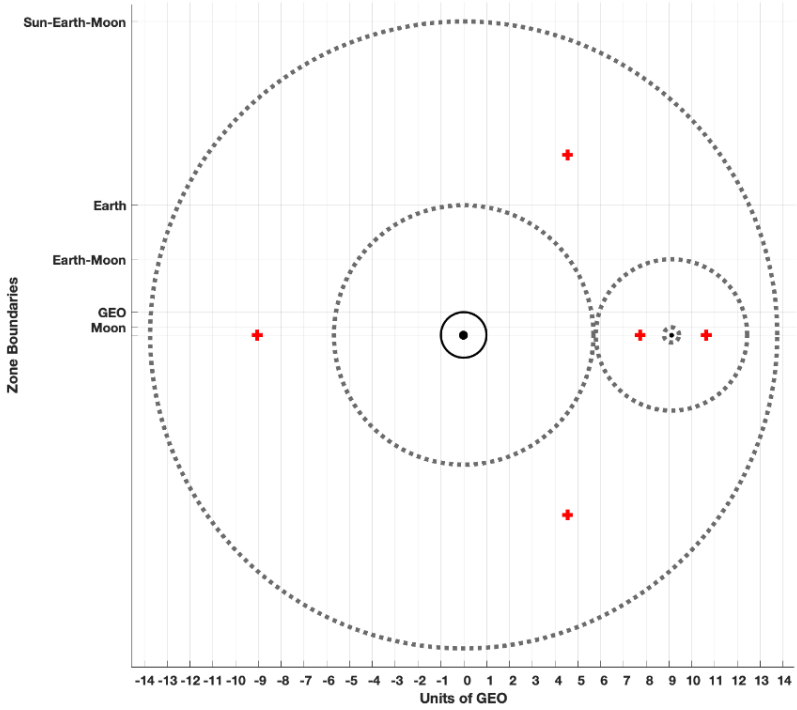

Figure 1. Spheres of influence of the Earth-Moon system with Lagrange points [2].

about 5.5xGEO) can be well approximated by using Earth as the sole source of gravity, or the two-body model (2BP), while the space within the Earth-Moon SOI has to use three body dynamics to accurately model the trajectory of a test satellite. It is important to note, however, that these SOIs are defined arbitrarily, most probably by the percentage of the total acceleration of the bodies on a satellite. These spe-

cific definitions of SOIs were not used in this research effort but more as a guiding principle.

These spheres can also be loosely correlated with the Jacobi energy of the CR3BP [2]. The orbits within the Earth's SOI but above GEO, which will be referred to as simply xGEO orbits, may be the key to blending the advantages of the simplicity and predictability of near Earth orbits, while still having the geometric diversity to perform cislunar SDA.

Therefore, given that SDA sensors based in GEO are inadequate in observing cislunar targets due to lack of geometric diversity and far ranges, and cislunar sensors being unpredictable and hard to communicate with, xGEO orbits may provide a way to bridge the gap. They are closer in range to most cislunar orbits compared to GEO, but are still stable enough to be well approximated by Earth's two-body model.

1.1 Objectives

The first objective of the research is quantifying the error in Keplerian and CR3BP xGEO orbits compared to the full-body Ephemeris model. Orbits with different altitudes have to be defined in the xGEO domain, comparing the two body, CR3BP, and Ephemeris models. Using this, the error of using a 2BP or CR3BP model compared to the "truth", the Ephemeris model, can be found over a period of time.

The second objective is evaluating how well xGEO orbits can observe cislunar targets. This is done by using the same sensor and CONOPs for each orbit, so that the impact of the orbit radius can be analyzed. In addition, to account for the increase in distance between satellites as the radius increases, a way to account for this increase in distance is created through increasing the number of satellites in the constellation.

The third objective is how xGEO orbits can be used to perform inspection missions

at L_1. This is done by using the stable manifolds of an L_1 Laypunov orbit, and their bifurcations with each xGEO orbit. It is then possible to find the smallest Δt and Δv solutions for each orbit and compare their trajectories. The Δt refers to the time of flight from the xGEO orbit to L_1, and the Δv is the total change in velocity required to reach it. These solutions with the smallest Δt and Δv will be referred as the "minimum solutions," but are in no way the optimal solution for this system, but rather the smallest found using the CR3BP and stable manifolds of L_1.

1.2 Limitations

There are limitations in this work due to computational constraints. The biggest limitation is that only certain xGEO orbits have been chosen, and so not the entire solution space (half orbits like 2.5xGEO) is explored. There are also many other orbits in other orbit planes that can be used for SDA and inspection missions that this study did not have time to explore.

For the orbit analysis, the analysis time is limited to 60 days, or about two lunar periods. This is done after assessing that the overall effect from third-body perturbations from the Sun and Jupiter on the analysis would be minimal. However, satellite constellation missions often span years instead of months, and even if the effects are small, they may add up over time. The limitations of the observational analysis were focused on the lack of cases to account for the variations in the sensor to target distance. A SNR saturation CONOPs is implemented to mitigate these effects, but more test cases of constellations with different true anomalies and inclinations are needed to truly overcome the limitation. Lastly, the inspection mission analysis is limited by using the CR3BP instead of the full-body Ephemeris model, as well as not having a way to maintain the orbit using controls. Instead, the analysis stops when the stable manifold begins, including the perturbation off the Lyapunov orbit. The

solutions found in this study will be useful in future studies using numerical solvers and optimizers like GPOPS-II or some equivalent optimal control program to find these trajectories.

1.3 Implications

Despite these limitations, this study of xGEO orbits is an important foundation for novel orbits not well researched in existing literature. These research objectives may lead to the consideration of xGEO orbits when designing cislunar SDA architectures. If the orbit shape is easy to maintain, is relevant and useful to cislunar SDA, and has the ability to perform inspection missions, it will be an important part of any such architecture.

1.4 Summary and Thesis Overview

In Chapter II, previous research into observability and cislunar topics are outlined and explored. Chapter III explains the simulation parameters of each objective and the specific metrics that the study analyzes. Chapter IV presents and analyzes the data and metrics described in chapter three. Chapter V will further interpret the results and presents possible future research.

II. Background

To accomplish the research objectives outlined in Chapter I, two main topics have to be explored, the topic of cislunar SDA and cislunar dynamics. First, a literature review of observational SDA performance metrics and constellation design is done, which serve as a basis to evaluate this research effort's study on xGEO observations. Then, differential corrections, periodic orbits, and manifolds are discussed, as they form the basis of the Lyapunov orbits in the third objective.

2.1 Cislunar SDA

In literature, there exist a few different ways to measure how well an orbit can perform its observations, using observation gramians and other heuristics. In addition, the trade space of different orbits in cislunar space are explored for use in SDA.

2.1.1 Performance Heuristics.

According to Fowler et al. [4], an objective way to measure the "degree of observability" from a single orbit can be calculated using the local observability gramian. It measures "the extent to which small perturbations to the initial conditions of a given trajectory create changes that appear in available measurements" [4]. It is defined as

$$P(x^0) = \int_0^T \kappa'(t)H'(t)H(t)\kappa(t)\mathrm{d}t. \tag{1}$$

Here κ represents the linear dynamics around the orbit, x^0 is the state vector anywhere in the trajectory, and H is the measurement Jacobian. However, these often result in numbers to compare orbits but does not provide any insight to the observation itself.

There are also many heuristics that can be used to evaluate the observability of an orbit that may be more intuitive. Three that Fowler et al. [4] used are angular rate,

geometry, and range. First, the angular rate between the object of interest and the observer is highly important since optical sensors need sufficient changes in position between observations. Without a long enough arc, the orbit determination for the object cannot be made. Therefore, the inverse relative angular rate would be a metric where a higher number means a worse observation.

A second metric that Fowler et al. [4] analyzed is the percentage of simulation time that the object is unavailable for geometric reasons. In cislunar space, where objects can be behind the Moon or Earth, unavailability can also be caused by other phenomena, such as occultation, Sun exclusion angles, and more. These phenomena can be seen in Fig. 2, diagrammed in the synodic frame as the Moon rotates around. Objects can be blocked by the Moon, or even be in between the observer and the Sun, making it unavailable to observe. Again, the lower the metric is, the better or more attractive the orbit analyzed is.

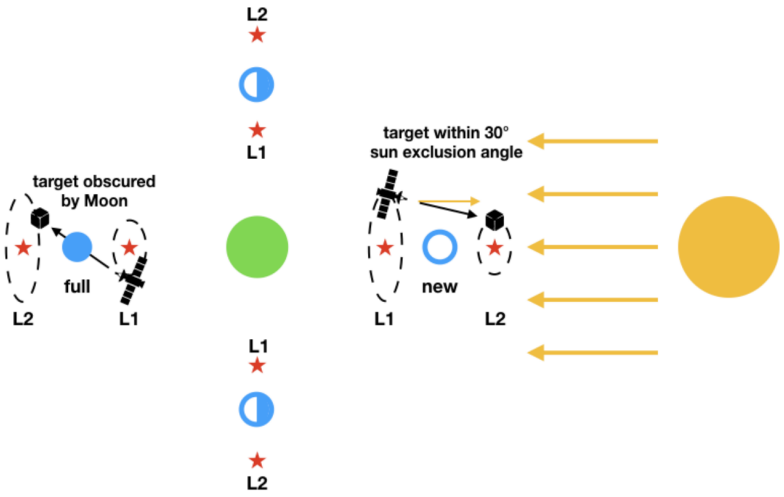

Figure 2. Geometric considerations for SDA performance [4].

Lastly, the range to the object of interest has to be considered. For optical sensors, the signal decreases as $1/r^2$, and the power received for radar based sensors decreases as $1/r^4$. The further away the object is, the more it will negatively affect observability.

Using these metrics, Fowler et al. ran simulations for a range of different observer and target orbits, as shown in Fig. 3. The way these metrics are defined, lower values represent better observability from the given orbit. For example, it can be seen that the L_4 planar orbit is consistently the easiest orbit to observe for the majority of the listed observer orbit families, perhaps besides from L_2. This makes sense, since L_4 can be clearly viewed from Earth and L_1, as seen in the definition of the Lagrange points. On the other hand, the range metrics on the L_4 planar orbits are often much larger than the other orbits, being further away from the Earth than the Moon.

	Target orbit family									
	L1 halo		L2 halo		L1 Lyapunov		L2 Lyapunov		L4 planar	
Observer orbit family										
Keplerian Earth	86%	3%	117%	4%	96%	3%	108%	3%	102%	1%
	20%	18.5	21%	20.4	14%	17.7	13%	16.4	14%	13.9
Keplerian Moon	15%	2%	17%	2%	35%	1%	28%	1%	107%	11%
	23%	18.8	24%	20.1	18%	17.6	14%	16.7	17%	13.9
L1 halo	1%	2%	31%	19%	34%	16%	33%	28%	101%	37%
	0%	18.5	21%	20.2	16%	17.6	14%	16.8	12%	13.9
L2 halo	31%	19%	1%	2%	42%	34%	30%	14%	117%	54%
	15%	18.9	2%	19.9	17%	17.5	9%	16.7	11%	13.8
L1 Lyapunov	28%	14%	39%	30%	41%	1%	46%	19%	102%	27%
	10%	18.4	16%	20.1	13%	17.4	14%	16.8	18%	13.8
L2 Lyapunov	34%	22%	27%	13%	51%	27%	35%	16%	115%	51%
	13%	18.9	13%	20.0	14%	17.7	18%	16.6	11%	14.1
L4 planar orbit	139%	2%	159%	5%	141%	2%	155%	4%	77%	1%
	14%	18.8	15%	20.1	13%	17.2	16%	16.9	14%	13.9

Key:	worst quartile	range (% avg Earth-Moon distance)	angular interval (% day)
	middle quartiles	inavailability (% simulation time)	empirical observability
	best quartile		

Figure 3. Comparison of different observer and target orbits [4].

There may not be any inherent correlation between the local observability gramian and any of the three heuristics that may be more intuitive. This may be due to the observability gramian taking into account the changing dynamics of the CR3BP, such that any small perturbation in initial conditions will lead to worse observation

conditions.

2.1.2 Constellation Trade Space for SDA.

Bolden et al. [3] explored three different challenges that observing cislunar space suffers— low signal to noise ratios, orbit instability of the observing constellation, and too-short-arc problems. Using these challenges as metrics to evaluate different CONOPs and constellations, Bolden et al. leveraged this information to explore the trade space for using cislunar space for SDA.

There are many geometric challenges to observing cislunar space, the biggest being low SNR and solar exclusion angles. As seen in Fig. 4, due to low solar phase angle (therefore negatively affecting the SNR), a LEO constellation cannot observe the majority of cislunar space, as is shown by the circle on the left side of Earth denoting revisit count. Due to the lack of geometric diversity, the entire constellation being too close to Earth meant that most of the desired coverage is unavailable due to low solar phase angle. The main driver for this is the size of the cislunar domain— the larger the domain, the lower the revisit rates will be. In addition to the revisit rate analysis, there will also exist Sun exclusion zones that are never available for coverage, as seen by the orange cone on the right side of Earth in Fig. 4. To improve the revisit rate count in geometries already observable, the number of observers can be increased, but this does not improve the unobservable domains. To do so, architectures have to have greater observation diversity by varying the geometry of the observers' orbit. This provides the motivation for using cislunar orbits for SDA. Not only does this give greater diversity and more chances to avoid exclusion zones, but also gives a closer range to objectives, giving a higher SNR.

The question is then, what type of architecture/orbits minimizes the gaps in coverage from only Keplerian orbits around Earth? This analysis, according to Bolden

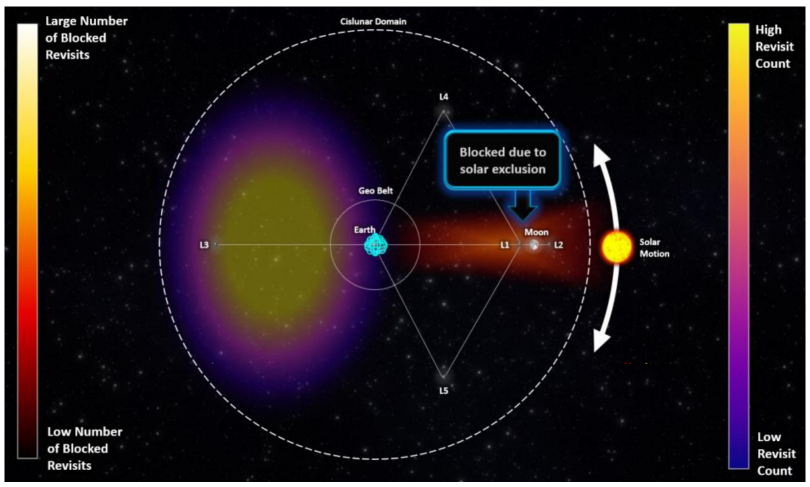

Figure 4. Solar exclusion angles and solar phase angles block revisit counts [3].

et al., can be done by simulating how different architectures fare against a free lunar return trajectory during the waxing crescent of the Moon, since "it is representative of the most challenging trajectories, primarily due to vast distances and poor solar phase angle conditions" [3]. The simulations were done by selecting the observer with line of sight to the object and had the highest SNR, which is then given "custody" of the object. The simulation used a 42cm telescope with a 1.8 degrees field of view in the visible spectrum [3]. The object of interest is assumed to be "a diffuse sphere with an albedo of 0.17 and a surface area of 1 m^2" [3].

An architecture consisting of GEO orbit regimes with various high inclination orbits, as well as three Lagrange point orbits at L_1, L_2, and L_5 is created, as seen in Fig. 5. With this architecture analyzing an object on a free lunar return trajectory, a simulation is run and the SNR and detection results are displayed in Fig. 6. The detections at the beginning and end of the simulation are from the observers at GEO, while the rest are at the Lagrange points. This architecture is a significant improvement over an architecture with just a GEO orbit, with less than 3 days of insufficient SNR to observe the object. To further close the gaps, Bolden et al. also added in other orbits at different Lagrange points and chaotic orbits, which have their

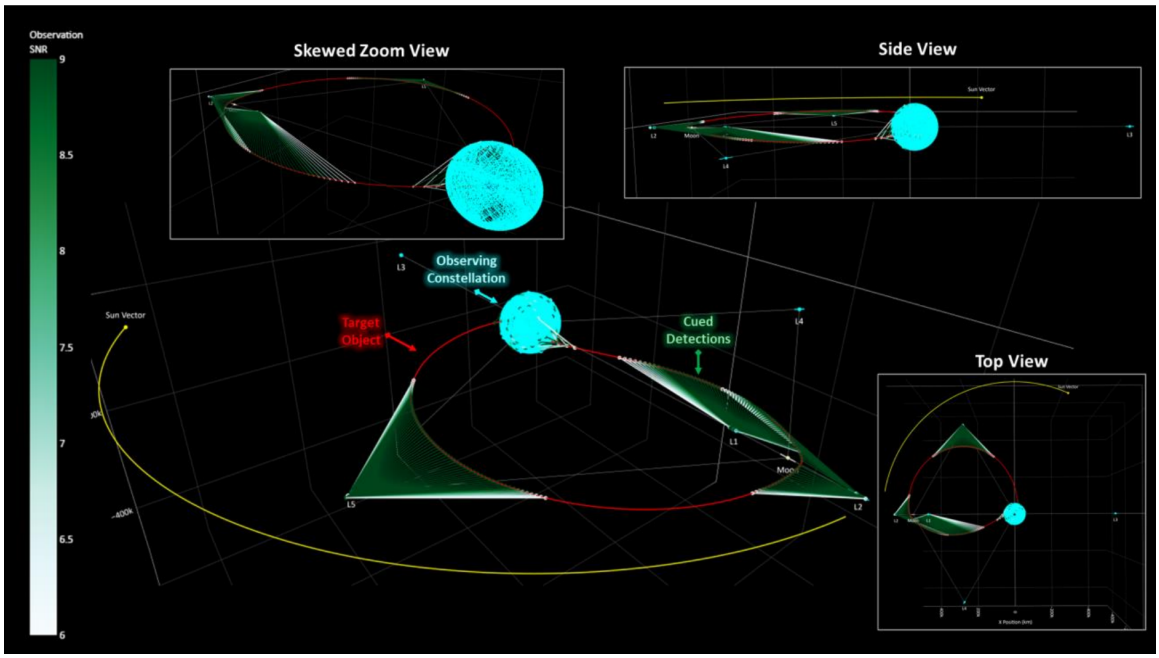

Figure 5. Model of the GEO + Lagrange point architecture [3].

own trade spaces [3]. Providing consistent coverage for the entire simulation time proved challenging, but provided a proof of concept of leveraging varied orbits to improve challenges from SNR and geometry. However, the Lagrange point orbits and chaotic orbits may present other challenges in orbit stability that offset its advantages.

The three-body problem is naturally complex and chaotic, and orbit parameters may vary wildly especially close to the Moon. The Moon may cause an Earth reentry scenario for some orbits if not properly monitored, but it may also create equilibriums like the Lagrange points [3]. Any orbit stability analysis has to be done throughout the lifetime of the orbit. Fig. 7 shows the periapsis altitude in terms of Earth radii over the span of three years, with green being a chaotic orbit, and black being a stable orbit (a P/3 orbit). Regardless of stability, the periapsis has variations throughout its lifetime, but it can be seen that the chaotic orbit has much larger changes [3].

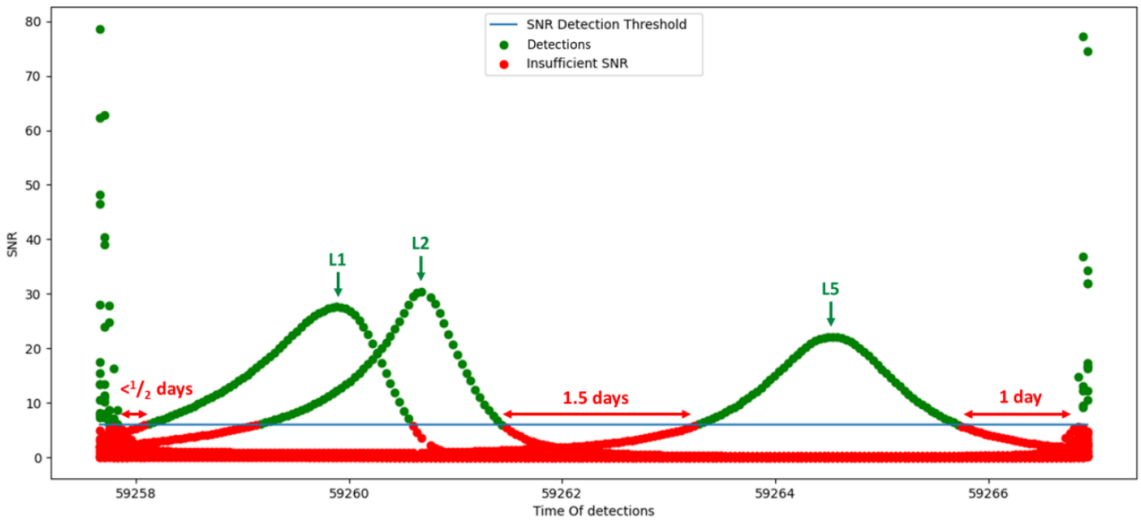

Figure 6. GEO + Lagrange point architecture SNR results [3].

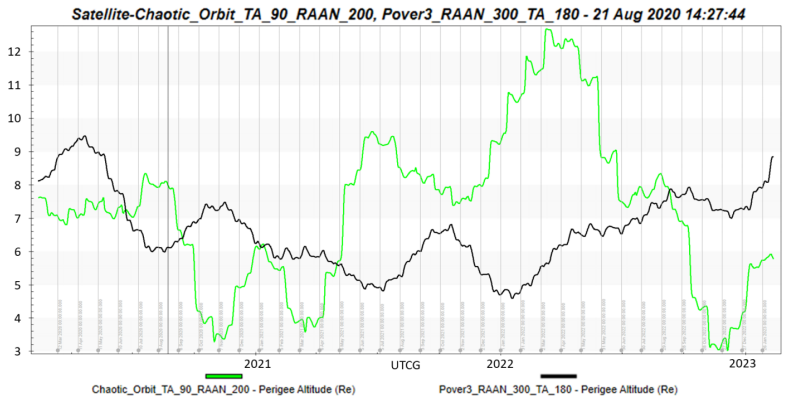

Figure 7. Rapidly changing RAAN for chaotic orbits [3].

In Fig. 8, the difference between a stable (cyan) and unstable (yellow) orbit is shown. The left side depicts the two orbits in the ECI frame, the Earth-Centered Inertial frame centered on Earth and the x axis fixed to the Vernal Equinox. The right side is in the rotating synodic frame, where the x axis rotates with the motion of the Moon such that the Moon is motionless in that frame. The unstable orbit is wildly varying and has no apparent pattern in the synodic frame, and therefore relies on numerical precision in computers to compute its future position. Meanwhile, the stable P/3 orbit stays inside one of the three "propellers" at any point in time, giving

a very predictable and consistent orbit for use in SDA. In addition, stable orbits are often stable for many years; when NASA's IBEX satellite entered the P/3 orbit it is estimated to stay in that orbit for at least 50 years [3].

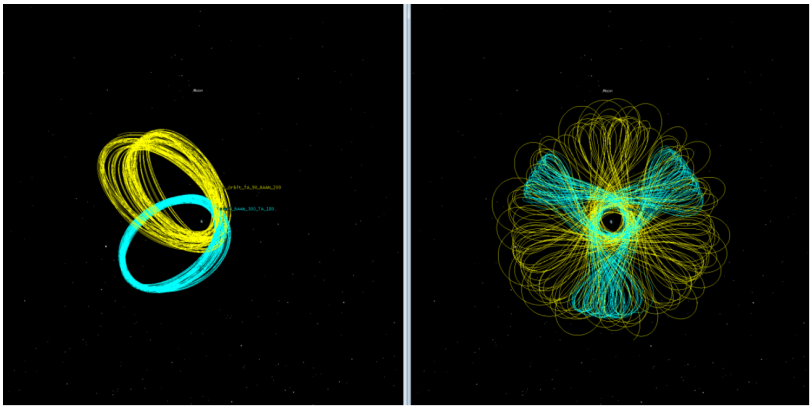

Figure 8. Orbit stability of the chaotic orbit and P/3 resonant orbit [3].

Lastly, the too short arc (TSA) problem happens when the observations over an orbit are too short in arc-length. This happens as a result of long time spans and limited observations. This is exacerbated in the cislunar domain due to the large ranges between objects and poor illumination/solar angles, which in turn requires more observations to create an accurate orbit determination.

This problem can be mitigated by defining an admissible region in range ρ and range rate $\dot{\rho}$ for a set of observations. This way of addressing the problem is much harder in cislunar space because of the chaotic 3BP dynamics, which make it harder to create the constraints defining the admissible region. In Bolden et al.'s analysis, ρ and $\dot{\rho}$ were limited by "investigating the geometric diversity introduced by the candidate observer constellations," that is to say, what the observer constellations could observe [3]. In addition, a 1,000,000 km length cube centered at the Earth's center is defined as the domain, and 3,375,000 reference points were evenly distributed throughout. "Two time-steps were modeled at one hour apart for each observer performing cued tracking vs the free lunar return trajectory during waxing crescent," the same object

of interest orbit as done before [3].

The results of the simulation, in an attempt to see how the TSA problem affects uncertainty, can be seen in Fig. 9. Although not shown here, the inclined GEO architecture performed much better than the LEO architecture; this is expected, since the range to the target has decreased while geometric diversity has increased. Despite the improvement, the uncertainty due to arcs being too short is still in the tens of thousands of kilometers.

Having a constellation of Lagrange point observers, the results of which are in Fig. 10, the uncertainty volume is much smaller than the GEO or LEO architectures. While this is encouraging, these graphs alone do not give the full picture since this simulation does not include SNR or the stability of the orbits. Once SNR is included, the uncertainties will significantly increase, due to the large ranges in the Lagrange point orbits compared to LEO or GEO. For example, any observer in L_3 is very unlikely to see the object on this free return trajectory as it will be too dim.

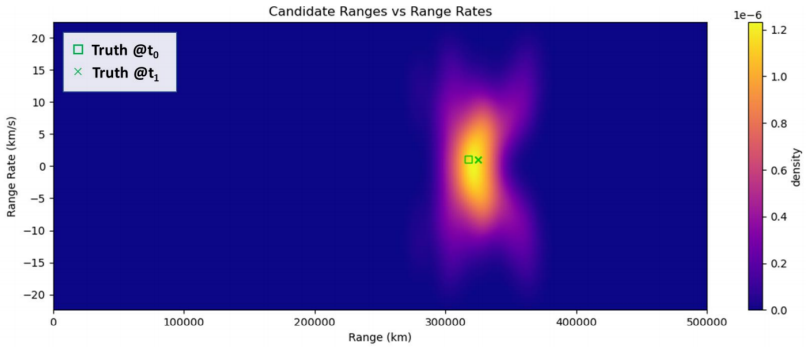

Figure 9. Range and range rate uncertainties for an inclined GEO architecture [3].

These three challenges, low SNRs, orbit stability, and TSA problems, are very important to consider when using cislunar space for SDA. Addressing these problems often involve either increasing the number of observers or adding more orbits to introduce more geometric diversity to the architecture. The Lagrange point orbits were heavily explored in all three topics, and often outperformed all the other orbits,

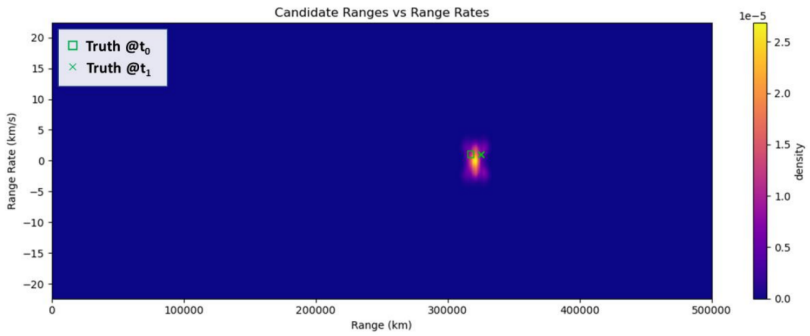

Figure 10. Range and range rate uncertainties for a Lagrange point architecture [3].

but by itself lacks the full geometric diversity needed to give persistent coverage of a challenging trajectories like the lunar free return.

2.2 Differential Corrections

Differential correction is the method of changing the initial conditions such that the constraints given are satisfied [5]. Using the calculus of variations, it is possible to correct a path that does not satisfy constraints to one that does through an iterative process. This procedure will be important in the discussion of forming cislunar periodic orbits, since the orbits are based on a targeting scheme that relies on differential correction.

2.2.1 State Transition Matrix.

The state transition matrix (STM), $\Phi(\tau + t_0, t_0)$, is a linear mapping of the error vector that allows for implementation of the differential corrector. Starting with the first order variational equations and the state vector $\vec{q} = [x, v]^T$ of position and velocities, the vector differential equation can be derived [6],

$$\delta\dot{\vec{q}} = A(t)\delta\vec{q} \tag{2}$$

where $A(t)$ is the Jacobian matrix of the dynamics of the system and $\dot{\vec{q}}$ is the time derivative of the state vector. In general, A is not a constant matrix, and has to be numerically integrated to a specific position and time within the orbit. However, if the reference orbit is periodic, then the matrix A is also periodic. The form of this matrix is six by six, since the corrective state is a six dimensional vector describing the difference between the reference orbit and the "actual" orbit. This matrix A is defined as

$$A = \begin{bmatrix} 0 & 0 & 0 & 1 & 0 & 0 \\ 0 & 0 & 0 & 0 & 1 & 0 \\ 0 & 0 & 0 & 0 & 0 & 1 \\ U_{xx} & U_{xy} & U_{xz} & 0 & 2 & 0 \\ U_{yx} & U_{yy} & U_{yz} & -2 & 0 & 0 \\ U_{zx} & U_{zy} & U_{zz} & 0 & 0 & 0 \end{bmatrix} \tag{3}$$

where U_{ij} is the second partial derivative of the potential function, $U_{ij} = \frac{\partial^2 U}{\partial i \partial j}$. It can again be shown [6] that the STM is propagated by the following differential equation,

$$\dot{\Phi}(\tau + t_0, t_0) = A(\tau)\Phi(\tau + t_0, t_0). \tag{4}$$

The numerically integrated STM can now be used to propagate the differential correction state through time,

$$\delta\vec{q}(\tau + t_0) = \Phi(\tau + t_0)\delta\vec{q}(t_0). \tag{5}$$

The STM numerically integrated through a full period for a periodic orbit is called the monodromy matrix, $M(t_1) = A(x(t_1), T_1)$. The eigenvectors of this monodromy matrix are important to the discussion of manifolds because purturbing in the direction

of the eigenvectors and integrating will result in the manifolds.

2.2.2 Contemporaneous and non-Contemporaneous Variations of the State.

The use of calculus of variations is extremely important in any targeting scheme, and will be used for the generation of periodic orbits. Following the development in Grebow [6], assume some current path x' and a reference path that follows the constraint given, x. Also assume that the six dimensional state vector $\vec{q}_i$, including the three dimensions of position and three dimensions of velocity, has some mapping f to the next state $\vec{q}_{i+1}$, such that

$$\vec{q}_{i+1} = f(\vec{q}_i, \Delta\tau)$$

where $\Delta\tau = \tau_{i+1} - \tau_i$.

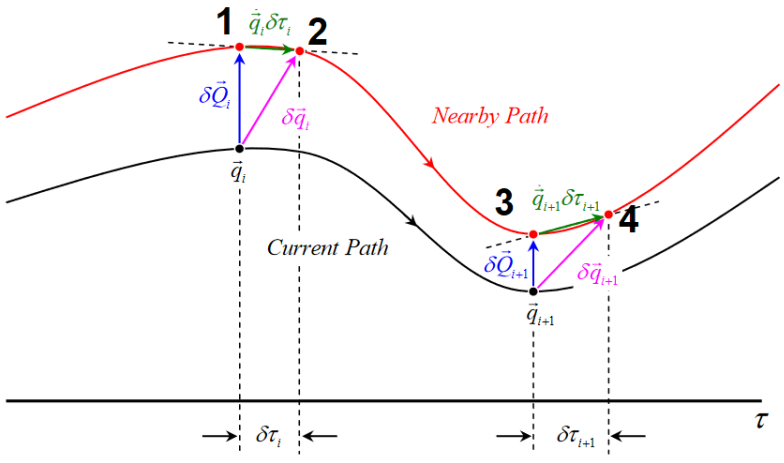

Figure 11. Variational definitions [6].

Following Fig. 11, it can be seen that to get the non-contemporaneous (time-

varying) state variation, $\delta\vec{q}_{i+1}$ has to satisfy

$$\vec{q}_{i+1} + \delta\vec{q}_{i+1} = f(\vec{q}_i + \delta\vec{Q}_i, \Delta\tau + \delta\tau_{i+1}), \tag{6}$$

where $\delta\vec{Q}_i$ is the contemporaneous (non-time varying) variation in the state on the i^{th} point. That is to say, using the dynamics embedded in f, the state can be mapped from point 1 to point 4 on the "nearby path" that follows the constraints given. If a Taylor expansion is done on f, a linear mapping of the generally nonlinear dynamics can be found,

$$\vec{q}_{i+1} + \delta\vec{q}_{i+1} = f(\vec{q}_i, \Delta\tau) + \frac{\partial f}{\partial \vec{q}_i}\Big|_{\vec{q}_i,\Delta\tau} \delta\vec{Q}_i + \frac{\partial f}{\partial \tau}\Big|_{\vec{q}_i,\Delta\tau} \delta\tau_{i+1}, \tag{7}$$

where higher-order terms are ignored for a first-order approximation. Redefining $\frac{\partial f}{\partial \vec{q}_i}\Big|_{\vec{q}_i,\Delta\tau} = \Phi(\tau_{i+1}, \tau_i)$ as the state transition matrix, and $\frac{\partial f}{\partial \tau}\Big|_{\vec{q}_i,\Delta\tau} = \dot{\vec{q}}_{i+1}$ as the derivative of the state at the timestep $i+1$, the linear approximation of the variational equations can be written as

$$\delta\vec{q}_{i+1} = \Phi(\tau_{i+1}, \tau_i)\delta\vec{Q}_i + \dot{\vec{q}}_{i+1}\delta\tau_{i+1}. \tag{8}$$

This equation, along with Eq. 5, give the important relational equation between contemporaneous and non-contemporaneous variations in state,

$$\delta\vec{Q}_i = \delta\vec{q}_i - \dot{\vec{q}}_{i+1}\delta\tau_i. \tag{9}$$

This relationship is also apparent in Fig. 11, going from the current path at point i to point 1. This serves as the basis for any targeting algorithm that does not depend on the initial time at the initial state, $\vec{q}_i$.

2.3 Periodic Orbits

Poincaré showed in 1892 that in the three body problem, there are infinite periodic orbits, although many solutions haven't been discovered yet. These periodic orbits are of particular interest because of their applicability in SDA. In the context of the CR3BP, there also exists quasi-periodic motion, where the orbit doesn't connect to its initial position but makes a similar shape in three-dimensional space.

First, the reference frame and equations of motion of the CR3BP is discussed. Then, a two-level corrections scheme is explored as a way to numerically create any periodic orbit in the CR3BP. Lastly, a few constraints are added to the corrections scheme to create Lyapunov orbits.

2.3.1 The Circular Restricted Three Body Problem.

As shown below in Fig. 12, a "synodic" reference frame is used, where the origin of the coordinate system is at the center of mass of the Earth-Moon system and the unit vector $\hat{x}$ will rotate along with the two bodies such that it points towards the Moon at all times. The Earth-Moon system is rotating around the center of mass in the plane spanned by the motion at a constant rate Ω given by

$$\Omega = \sqrt{\frac{G(m_1 + m_2)}{r_{12}^3}}.$$

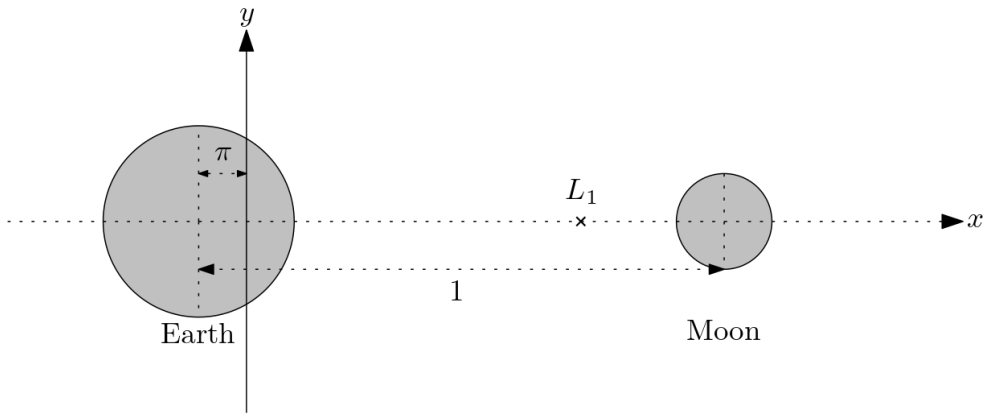

Figure 12. CR3BP Non-dimensionalized barycentric coordinate system.

For better numerical integration, non-dimensional units are also used. Scalar distances will be non-dimensionalized using $r_{12} = 384400$ km, the average distance between the Earth and Moon. The mass parameter is defined as

$$\mu = \frac{m_2}{m_1 + m_2}.$$

This allows us to use

$$m_2 = \mu, \quad m_1 = 1 - \mu,$$

if $m_1 + m_2 = 1$ is considered to be 1 mass unit. The coordinates of the primary and secondary can also now be described by

$$x_{\text{CM}} = \frac{m_1 x_1 + m_2 x_2}{m_1 + m_2} = (1-\mu)x_1 + \mu x_2 = 0 \Rightarrow x_1 = -\mu, x_2 = 1 - \mu \qquad (10)$$

since the center of mass is at the center of the reference frame. This can also be seen in Fig. 12. The gravitational constant G as well as the angular velocity $\tilde{\Omega}$ will be set to one, where the tilde represents the non-dimensional form. The time unit is $1/\Omega$ and the non-dimensional period $\tilde{P}$ will equal 2π. The equations of motion for a

synodic reference frame with the discussed non-dimensionalization is

$$\ddot{x} = 2\dot{y} + x - (1-\mu)\frac{x+\mu}{r_1^3} - \mu\frac{x-1+\mu}{r_2^3} \tag{11}$$

$$\ddot{y} = -2\dot{x} + \left(1 - \frac{1-\mu}{r_1^3} - \frac{\mu}{r_2^3}\right) y \tag{12}$$

$$\ddot{z} = -\left(\frac{1-\mu}{r_1^3} + \frac{\mu}{r_2^3}\right) z. \tag{13}$$

2.3.2 Two-level Corrections Scheme.

Given that there are no analytic solutions to orbits in the CR3BP, numerical solutions have to be used. Starting from the linearized dynamics, an initial guess can be created, but may only be accurate near the place of linearization (usually near a libration point). From this initial guess, differential corrections can be used to close the orbits, satisfying the constraints given by the CR3BP dynamics.

In Grebow, a two-level correction scheme is used [6]— first, discontinuous velocity states are enforced in favor of continuous positions throughout the orbit. That is, starting with a set of points to "patch" together, and an analytic guess of the states that connects them, this first level correction scheme can create a continuous orbit that may not have "smooth" curves. Fig. 13 below shows the disjoint internal patch points, where some Δv is needed to travel to the next arc, since it is smooth in position space but not in velocity space. This results in a v_i^+ and v_i^- at each patch point, representing the velocity at the end of the last arc and the initial velocity at the start of the i^{th} arc. The red lines denote the actual orbit that follows CR3BP dynamics, while the black lines represent the corrected orbit. A second level correction is then used to minimize the $\Delta v_i = v_i^+ - v_i^-$ needed to patch together the first level. This is shown in Fig. 14 where the black lines represent the result of the level one corrector, and blue lines represent the resulting level two Δv minimization. The positions of the patch points and the time it takes to reach there may be varied to minimize the

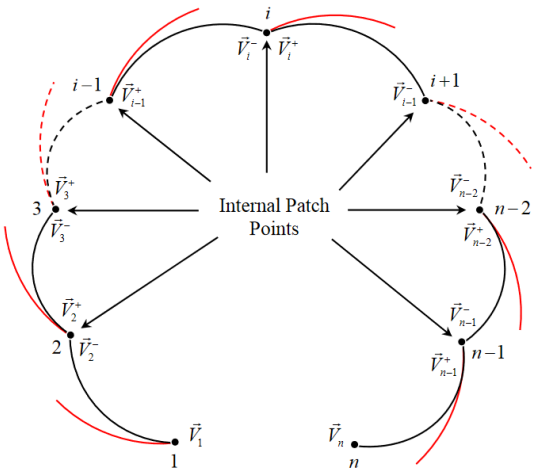

Figure 13. The first "level" of the correction scheme [6].

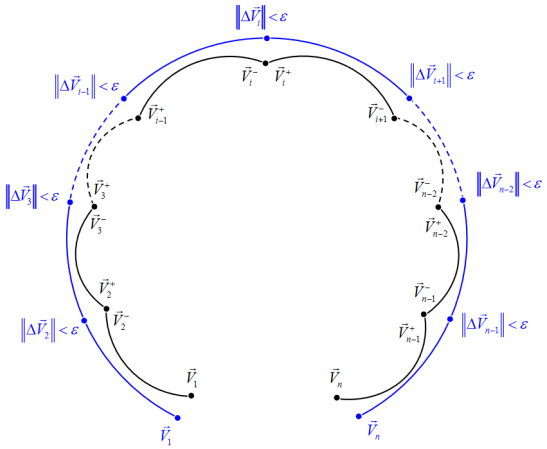

Figure 14. Second level of the corrector [6].

Δv. These two are repeated in order until the level of required Δv fidelity is reached in between each patch point [6].

The linear approximation for the variation of the ith trajectory between the actual and reference patch point is

$$\delta\vec{q}_{i+1} = \Phi(\tau_{i+1}, \tau_i)\delta\vec{Q}_i + \dot{\vec{q}}_{i+1}\delta\tau_{i+1} \tag{14}$$

as discussed in Section 2.2. This equation can be used to iteratively update the velocity and time such that the variation at the patch point will go to zero.

With $\vec{V}_i$ being the velocity associated with the ith patch point and τ_{i+1} the time of integration from the ith to the $i+1$th patch point, they can be repeatedly updated using

$$L = \begin{bmatrix} \frac{\partial x}{\partial \dot{x}_0} & \frac{\partial x}{\partial \dot{y}_0} & \frac{\partial x}{\partial \dot{z}_0} & V_{x,i+1} \\ \frac{\partial y}{\partial \dot{x}_0} & \frac{\partial y}{\partial \dot{y}_0} & \frac{\partial y}{\partial \dot{z}_0} & V_{y,i+1} \\ \frac{\partial z}{\partial \dot{x}_0} & \frac{\partial z}{\partial \dot{y}_0} & \frac{\partial z}{\partial \dot{z}_0} & V_{z,i+1} \end{bmatrix} \tag{15}$$

$$\begin{bmatrix} \delta\vec{V}_i \\ \delta\tau_{i+1} \end{bmatrix} = L^T(LL^T)^{-1}\delta\vec{R}_{i+1} \tag{16}$$

until $\delta\vec{R} < \varepsilon$ for some arbitrarily small ε, where $\delta\vec{R}$ represents the error in position. This corresponds to the difference between the end of the red lines and the next patch point in Fig. 13. As a result, each patch point will have a different initial velocity, and in general the patch points will have discontinuous velocities, one before the patch point, V_i^-, and the new initial condition found by the first level at that point, V_i^+. The $\Delta\vec{V}$ needed to connect to the next patch point is then the difference between the two,

$$\Delta\vec{V}_i = \vec{V}_i^+ - \vec{V}_i^-. \tag{17}$$

The second level involves making the $\Delta\vec{V}_i$ at each patch point as small as possible, such that the orbit closes and gives a "smooth", natural orbit. To do this, variations in $\Delta\vec{V}_i$ have to be expressed as functions of $\delta\vec{R}_i$ and $\delta\tau_i$ [6]. As seen in Eq. 17, the $\Delta\vec{V}_i$ is dependent on the velocities which are themselves dependent on the states and times. This minimization is again done by using calculus of variations, where the i^{th} variation of the velocity will be

$$\delta\Delta\vec{V}_i = \sum_{j=i-1}^{i+1} \left(\frac{\partial\Delta\vec{V}_i}{\partial\vec{R}_j}\delta\vec{R}_j + \frac{\partial\Delta\vec{V}_i}{\partial\tau_j}\delta\tau_j \right). \tag{18}$$

After some development [6], all of the needed partial derivatives in that expression can be expressed in terms of the integrated STMs $\Phi(\tau_{i+1}, \tau_i)$ and $\Phi(\tau_{i-1}, \tau_i) = \Phi(\tau_i, \tau_{i-1})^{-1}$, where one is expressed as the inverse so that integrating backwards in time is not necessary. For further detail, Grebow performs a more rigourous mathematical derivation [6]. As a result, a banded matrix M can be built such that it maps the position and time vector to the variations in $\Delta\vec{V}_i$,

$$\begin{bmatrix} \delta\Delta\vec{V}_2 \\ \delta\Delta\vec{V}_3 \\ \vdots \\ \delta\Delta\vec{V}_{n-2} \\ \delta\Delta\vec{V}_{n-1} \end{bmatrix} = [M] \begin{bmatrix} \delta\vec{R}_1 \\ \delta\tau_1 \\ \delta\vec{R}_2 \\ \delta\tau_2 \\ \delta\vec{R}_3 \\ \delta\tau_3 \\ \vdots \\ \delta\vec{R}_{n-2} \\ \delta\tau_{n-2} \\ \delta\vec{R}_{n-1} \\ \delta\tau_{n-1} \\ \delta\vec{R}_n \\ \delta\tau_n \end{bmatrix} \tag{19}$$

To enforce the smallest $\Delta\vec{V}_i$ at each patch point, the smallest Euclidean norm of the matrix M can be used to find the new set of patch points and times, by subtracting the $\delta\vec{R}_i$ and $\delta\tau_i$ found from this current iteration. Now that a new set of patch points and the $\delta\vec{V}$'s have been found, the first level is performed again, and is repeated until $|\Delta\vec{V}_i| < \varepsilon$ for $i = 2, \cdots, n-1$. This results in a continuous, "natural" orbit that is periodic.

This two-level corrections scheme is used in Grebow to create particular solutions to the nonlinear dynamics in the CR3BP. Applied to a linear approximation of a quasi-periodic trajectory near L_1, with 41 patch points, the total Δv summed over all points is reduced from 1.203 to 2.517×10^{-13} non dimensional units in only six iterations. This is used to create many families of orbits to select for lunar south pole coverage. Using the CR3BP model as an initial guess, a transition to a full ephemeris model including solar perturbations is done with the use of control and station-keeping techniques. Grebow used Astrogator Connect to calculate the station-keeping costs, which relied on differential correction techniques [6].

2.3.3 Lyapunov Orbits.

Constraints can be added to the two-level corrector to calculate the Lyapunov orbits near the collinear points. In general any symmetry introduced in a system will also simplify the dynamics, and it is also true in this case. If a x-z symmetry is introduced, the periodic, planar solutions that result near the collinear points are named the Lyapunov orbits [6].

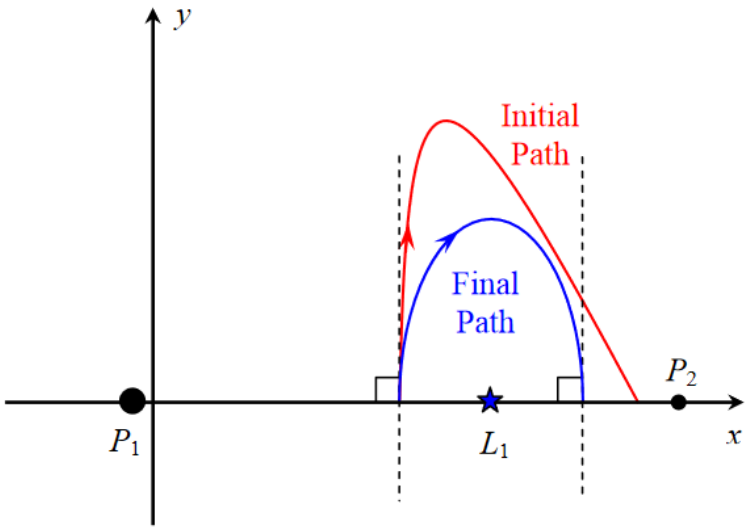

Figure 15. The simple corrector [6].

To get this x-z symmetry, the final point considered in the corrector is a half period (as seen in Fig. 15), and the initial and final conditions are enforced such that there is zero velocity in the x or z direction. To generate these orbits, start with the initial condition $\vec{q_0} = (x_0, 0, 0, 0, \dot{y}_0, 0)^T$ taken from the orbit linearized around the Lagrange point, and adjust the x_0 and $\dot{y}_0$ values such that the crossing of the x axis is also perpendicular with no $\dot{x}$ velocity.

Using differential corrections, it can be seen that

$$\delta\dot{x} = \frac{\partial \dot{x}}{\partial \dot{y}}\dot{y}_0. \tag{20}$$

Following the same steps as the two-level correction scheme, the $\delta\dot{x}$ at the final point it crosses the x axis can be minimized until it's less than some small scalar $\varepsilon > 0$. The resulting half-orbit is then the initial condition found with this simple corrector method integrated over its period 2τ, where τ is just the time it takes to get to its first crossing of the x axis. To get the neighboring solutions, step the position along the x axis (with the x_0 value in our initial conditions) with a fixed value Δx_0.

The numerical results of the Lyapunov orbits as described can be seen in Fig. 16. The black line is the "bifurcation", the intersections between the blue Lyapunov orbit family with other types of periodic orbits. Also notice that the final point of the targeting scheme breaks down as the final point gets closer to the Moon, and is generally true for when any of the primaries are close [6]. Eventually the steps taken from the initial conditions are large enough such that the resulting orbit will reach around the Moon, and become distant retrograde orbits (DROs).

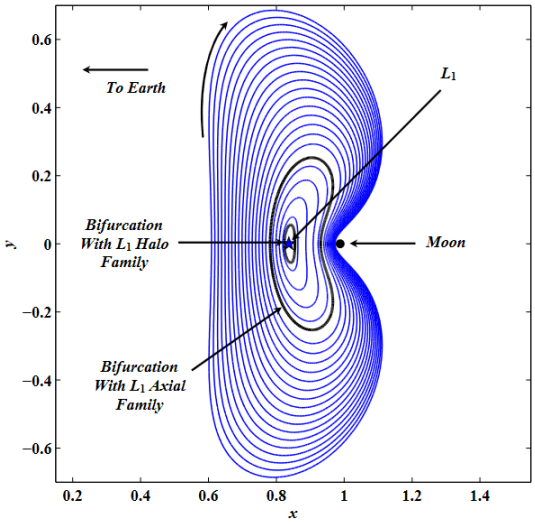

Figure 16. Lyapunov orbit family [6].

The stability of orbits rely on eigenvalues λ_i of the monodromy matrix evaluated over the orbit. Since the eigenvalues always appear in reciprocal pairs, a stability index can be defined as

$$\nu_i = \frac{1}{2}(\lambda_i + 1/\lambda_i) \quad \text{for } i = 1, 2.$$

If the absolute values of the stability index are less than one, then the orbit is marginally stable, and otherwise, the orbit is unstable.

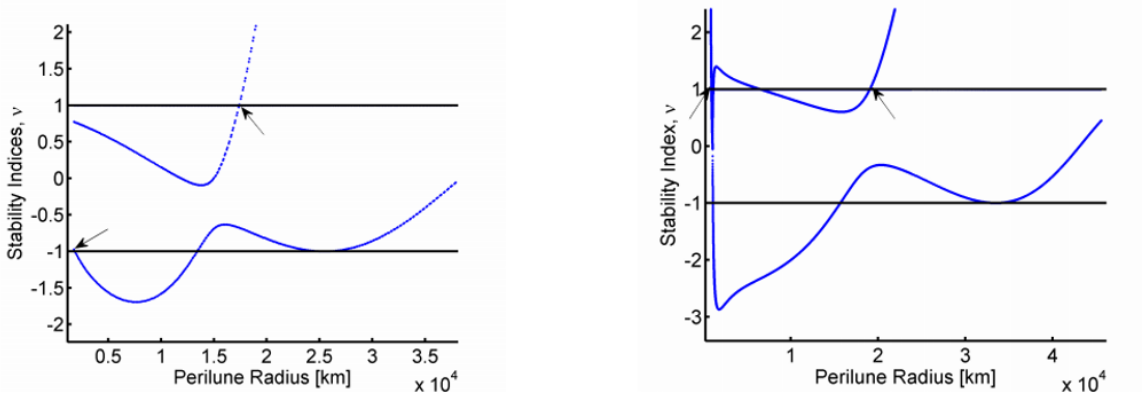

(a) Stability index across the L_2 halo family.

(b) Stability index across the L_1 halo family.

Figure 17. The stability indices as a function of the orbit's perilune radius [7].

This can be visualized in Fig. 17, where the arrows define the region that the orbit is stable. This kind of stability analysis may also be used for other orbits, and serves as a helpful indicator of stability.

2.4 Manifolds

Structures that contain possible paths to and from libration points without using any extra Δv are called manifolds, existing as a result of any unstable orbits. Perturbations from these unstable orbits will result in an orbit that leads exponentially away from the initial orbit [8]. Since these paths don't need any extra Δv, they serve as good initial guesses to minimize the fuel needed. Stable manifolds, denoted by W^S and the S superscript, give paths toward a libration point, while unstable manifolds, W^U and the U superscript, give paths away from a libration point.

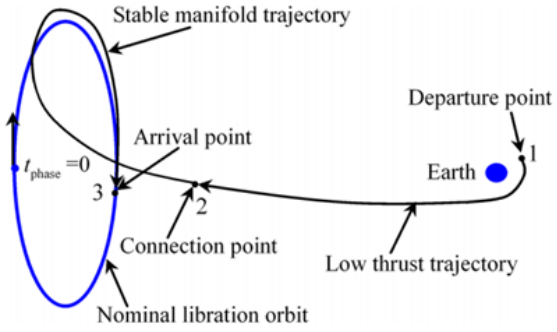

Figure 18. Creating a transfer using the manifolds [8].

As seen in Fig. 18, the basic structure of the orbital transfer using the manifolds are then constructed. Starting in an initial unstable periodic orbit, an exit point is selected and perturbed along the direction of the unstable manifold. When the unstable manifold the satellite is on connects with a stable manifold leading to the chosen libration point, a Δv is performed to perturb onto the stable manifold. Another Δv is needed once the satellite arrives on the stable periodic orbit. Since the perturbation on and off periodic orbits require the state transition matrix of the stable and

unstable periodic orbit, an exploration of how to get the state transition matrix is needed.

To use the manifolds, a point in the periodic orbit is first chosen. Then, the monodromy matrix is evaluated as described in Section 2.2.1 to find its eigenvectors at that point. The state at that point in the orbit is then perturbed along the stable or unstable eigenvector with a small parameter $\varepsilon > 0$. This constraint guarantees that it leaves the orbit without taking too long. [9]. The states can then be expressed as

$$q_0^S = q_0 \pm \varepsilon \frac{v^S}{|v^S|}, \quad q_0^U = q_0 \pm \varepsilon \frac{v^U}{|v^U|} \tag{21}$$

where the S and U denote the stable and unstable eigenvectors of the monodromy matrix $\Phi(\tau + t_0)$, respectively. Since the eigenvectors include the position and velocity, "perturbing" in that direction also includes perturbing the velocity as well. In addition, these eigenvectors will be dependent on the point in the orbit the satellite is entering or leaving, since in general the monodromy matrix will be different. In Fig. 19 for example, the chosen point is at t_1 after the initial state x_0 in the orbit.

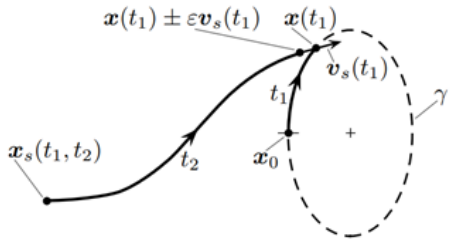

Figure 19. Linearizing the manifold near the orbit [10].

Fig. 19 shows how to get onto the orbit labeled γ with a Δv using numerical integration in t_2. The six dimensional position and velocity state is denoted by x, the stable manifold trajectory by x_s, and the stable eigenvector v_s.

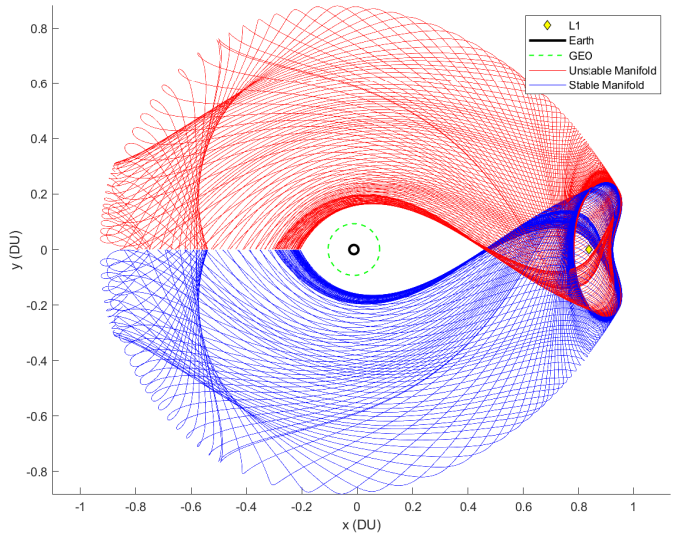

Figure 20. The stable and unstable manifolds of L_1.

One way to visualize the manifolds is by discretizing the points on the periodic orbit and integrating backwards/forwards in time to get their paths. The resulting image will be much like Fig. 20, where the stable (blue) and unstable (red) manifolds are shown around the L_1 Lyapunov orbit. The entire manifold can then be created by performing the same algorithm for each set of initial conditions in the orbit. In addition, the direction of perturbation (the $\pm$ in Eq. 21) will determine the direction the manifolds will move. The choice of sign will determine what direction the manifolds will face.

These manifolds have been used by many in literature as an initial trajectory guess to minimize fuel. In Peng et al. [8], a "mixed transfer approach" is used to design a transfer between a LEO orbit and a given Halo orbit. From LEO, a low thrust trajectory is used until it got onto a manifold that led to the Halo orbit. The low thrust trajectory is designed using optimal control, where one of the important constraints is that the end point had to be connected with the stable manifold. This can be seen at the red star in Fig. 21, the connection point between the low thrust

Table 1. Trade space between time of flight and ΔV [8].

Case	ΔT (days)	Δv (m/s)	Fuel saving (%)
1	219.899501	74.786315	38.54
2	190.762692	87.962795	32.91
3	118.972750	94.452848	32.72
4	70.629541	171.749195	15.09
5	49.976216	289.217941	14.24
6	29.989770	757.648784	3.93

trajectory and the stable manifold. This point is also a design variable to optimize for the time of flight Δt and Δv, as generally the more time spent on the manifold will mean a longer time of flight but a greater savings in Δv. As seen in Table 1 adapted from Peng, with the fuel saving column as compared to purely using low thrust during the entire trajectory [8].

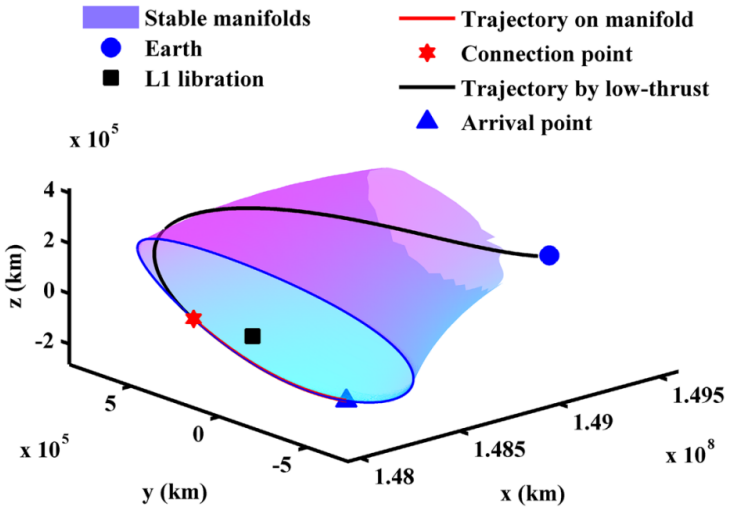

Figure 21. Mixed transfer approach of trajectory optimization [8].

Another recent use of these manifolds has been in the context of low thrust (LT). Given some constant, small thrust, the manifolds turn into "dynamical structures that pulsate with the varying Hamiltonian value" [11]. Since the Hamiltonian values change in time, the "zero velocity curves" that exist in the CR3BP are changed to "zero acceleration curves" within this model. The CR3BP libration points are also

moved to new points in this CR3BP + LT model, which may vary greatly depending on the direction of the constant thrust. Fig. 22 connects the stable (blue) and unstable (red) low-thrust manifolds between two low-thrust periodic orbits in the CR3BP+LT equivalent of the L_1 and L_2 points.

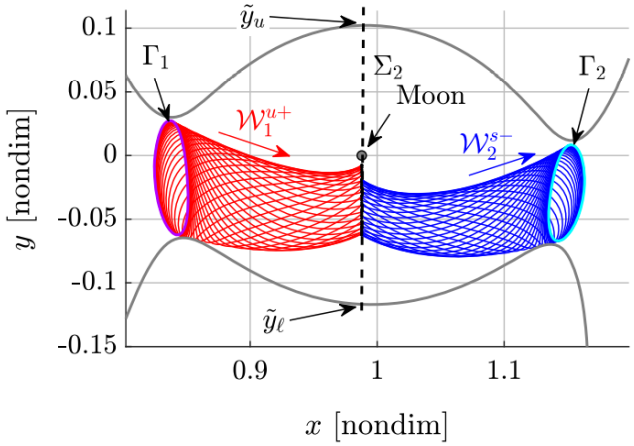

Figure 22. Manifold visualization [11].

2.5 Summary

This chapter reviewed the existing literature on performance heuristics of observational satellites, the trade space of using traditional LEO/GEO orbits vs cislunar orbits for cislunar SDA, how to create Lyapunov orbits using differential correction, and the dynamics of the CR3BP. The literature review helps define the research effort, detailed in the next chapter, Methodology.

III. Methodology

This chapter explores how MATLAB and STK were used to analyze the use of xGEO orbits. First, a combination of MATLAB and STK were used to create xGEO orbits and simulate their trajectories using different models, from only including the Earth to including the other planets in the Solar System. Then, these xGEO orbits are modeled in STK as Keplerian orbits and their use as observation orbits are explored. Finally, the CR3BP model of stable manifolds coming from L_1 are used to create trajectories from xGEO orbits to L_1 Lyapunov orbits to show the xGEO orbits' use for inspection missions.

3.1 Orbit Analysis

To explore the validity of xGEO orbits, first an analysis of how much low to mid fidelity models can approximate a high fidelity one. This is done by comparing three different models of xGEO orbits— using the full-body Ephemeris model as the truth, and the circular restricted three body and two body models to compare. This requires generating each case from the same initial conditions, and then comparing how their positions differ over time.

The altitudes to try were arbitrarily cut off at 5xGEO, due to the increasing effect the Moon would have on the orbit and to limit the computation time required to do the analysis. As seen in Fig. 23, at 5xGEO the Moon's gravitational acceleration is already approaching 1.5% of Earth's and can have significant effect on the orbit trajectory.

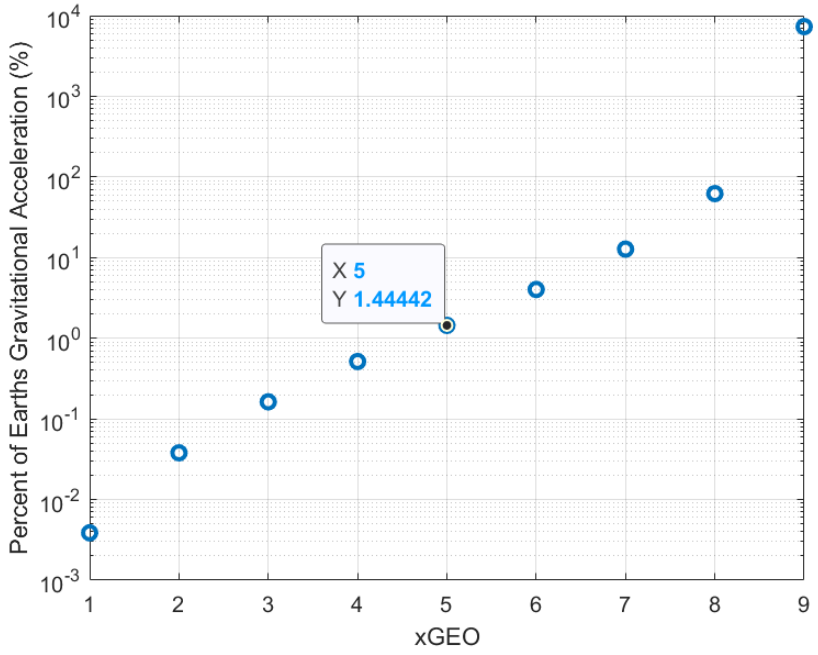

Figure 23. Moon's perturbation compared to Earth's gravitational field.

The main factors of consideration for simulation time are the positions of the Moon and Sun, the two being the primary sources of gravitational perturbation in the Ephemeris full-body model, as shown below in Fig. 24. In this graph, where the y axis is on a log scale, the satellite experiencing the acceleration is modeled at 1, 3, 5, and 7xGEO in the direction of the Moon from Earth. The non-inertial force from the accelerating Earth-centered frame is added to each perturbation, such that

$$\vec{a}_{i,\text{eff}} = \mu_i \left(\frac{\vec{r}_i - \vec{r}}{|\vec{r}_i - \vec{r}|^3} - \frac{\vec{r}_i}{|\vec{r}_i|^3} \right), \tag{22}$$

where $\vec{r}_i$ is the position vector from Earth to the perturbation, $\vec{r}$ is the position vector from Earth to the satellite, and μ_i is the mass parameter of the perturbation. The first term represents the inertial gravitational force, and the second term is the non-inertial force that comes from the Earth-centered frame of reference being accelerated by object i.

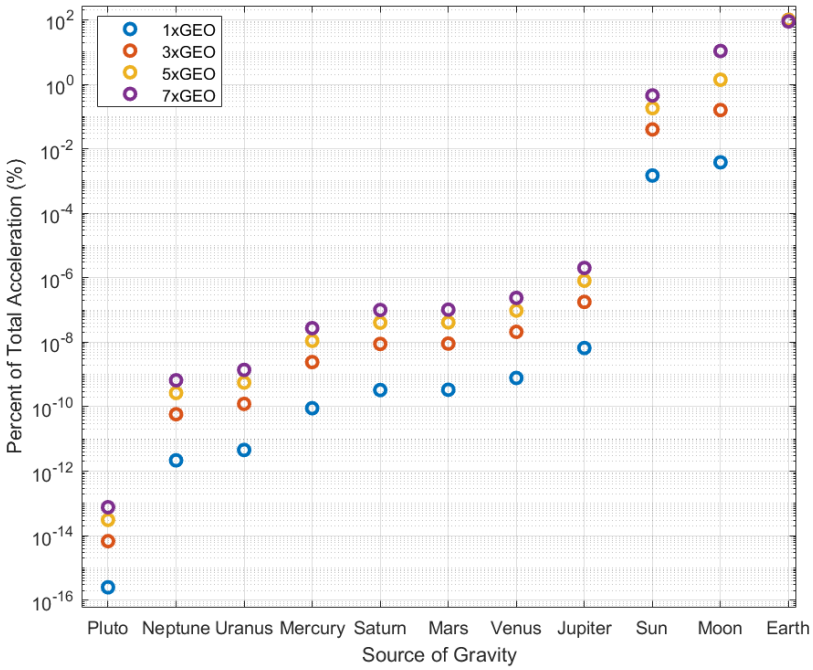

Figure 24. Percent of total acceleration from each gravitational source in the Earth-centered ICRF.

While the Sun as a secondary perturbation has some impact on the trajectory, when taken over multiple orbit periods, the impact on the trajectory will be negligible. Given this assumption, we can start the simulation at an arbitrary date as long as it spans over multiple lunar periods, since it's the other major source of possible trajectory error. Therefore, January 1st, 2021 is chosen as the arbitrary start date, and the analysis is done over sixty days, or about two lunar periods.

3.1.1 Models.

For the Ephemeris model of satellites in xGEO orbits, the STK's Astrogator tool is used, which takes into account the gravitational attraction of all the bodies in the solar system, including the Sun and asteroids. The Earth is chosen as the center, and all vectors are represented in the International Celestial Reference Frame (ICRF), which is fixed to the stars. Since this reference frame is indepedent of the ecliptic

plane, all future reference to the x-y plane is referring to this ICRF.

The Ephemerides DE421 model is used in both STK and MATLAB for consistency, so that MATLAB's `planetEphemeris` function could be used. This function allows a Julian date to be defined, then accesses JPL's ephemeris data to output the positions and velocities of any body with respect to another.

To model the CR3BP, instead of attempting to rotate into the plane of the Moon's orbit from the ICRF, a circular orbit created from the Moon's initial condition taken from the ephemeris data. This is done by getting the initial position and velocity from `planetEphemeris`, then using cross products to find the tangential direction of motion. This is then scaled by the average velocity of the moon at its average radius of its orbit, defined as 384,400 km. In an equation, the circular position and velocity of the Moon, $\vec{r}_{M,c}$ and $\vec{v}_{M,c}$, are then

$$\vec{r}_{M,c} = r_{12}\frac{\vec{r}_M}{|\vec{r}_M|} \tag{23}$$

$$\vec{v}_\perp \equiv (\vec{r}_M \times \vec{v}_M) \times \vec{r}_M \tag{24}$$

$$\vec{v}_{M,c} = \sqrt{\frac{\mu_\oplus}{r_{12}}}\frac{\vec{v}_\perp}{|\vec{v}_\perp|} \tag{25}$$

where $\vec{r}_M$ and $\vec{v}_M$ are the given position and velocity of the Moon from `planetEphemeris`, $\mu_\oplus = GM_\oplus$ and $r_{12} = 384400$ km, and $\vec{v}_\perp$ is a vector tangent to the circular orbit at radius r_M. Then, treating the Moon in this assumed circular orbit as a third-body perturbation of Earth's gravity, the total acceleration of a satellite is

$$\ddot{\vec{r}}_{\text{sat}} = -\frac{\mu_\oplus}{r_{\text{sat}}^3}\vec{r}_{\text{sat}} + \mu_M\left(\frac{\vec{r}_{M,c} - \vec{r}_{\text{sat}}}{|\vec{r}_{M,c} - \vec{r}_{\text{sat}}|^3} - \frac{\vec{r}_{M,c}}{r_{M,c}^3}\right). \tag{26}$$

This is then numerically integrated with `ode113` with the same timesteps as the Ephemeris model.

Lastly, the Keplerian two-body orbit is created as a circular orbit with the same

timesteps as the Ephemeris model. This, as well as the CR3BP model, is created with the same timesteps to be able to compare the error correctly— otherwise comparisons between different timesteps would distort the results. Therefore, the two body position and velocity vectors are

$$\nu = 2\pi \left(\frac{t_{\text{Eph}}}{\mathbb{P}} \right) \tag{27}$$

$$\vec{r}_{2BP} = r_{12} \begin{bmatrix} \cos\nu \\ \sin\nu \end{bmatrix} \tag{28}$$

$$\vec{v}_{2BP} = \sqrt{\frac{\mu_\oplus}{r_{12}}} \begin{bmatrix} -\sin\nu \\ \cos\nu \end{bmatrix} \tag{29}$$

where t_{Eph} is the array of timesteps given by STK's Ephemeris model and $\mathbb{P}$ is the period of the orbit given by $\mathbb{P} = 2\pi\sqrt{r_{12}^3/\mu_\oplus}$.

3.1.2 Metrics.

The particular metric of interest is how far apart the propagated positions of each satellite are from each other over time in each model. However, the larger velocities and third-body perturbations in higher altitudes also increases the errors. Therefore, the errors are better represented as percentages of their radius,

$$\tilde{e} = \frac{e}{R} \tag{30}$$

where e is the true error in km, R is the orbit radius, and $\tilde{e}$ is the fractional error.

The other metric of interest is the instantaneous true anomaly relative to the initial condition. This is an accompanying metric to the first one to see how much of the error is "in track". To do this, the `vrrotvec` function in MATLAB is used to find the angle between two vectors— the initial position vector and the current position

vector. The output of the function is a rotation vector and an angle, such that when $\theta > \pi$, the angle is wrapped to $[0, \pi]$ and the rotation vector is flipped to negative z. To account for this, another term is applied to the output of the function,

$$\nu = 2\pi(z < 0) + (-1)^{(z<0)}\nu_{\text{out}} \tag{31}$$

where ν_{out} is the angle given by `vrrotvec` and $(z < 0)$ is 1 when the z is negative and 0 when z is not negative. This ensures that when the rotation vector is in the negative z direction, the angle is $\nu = 2\pi - \nu_{\text{out}}$, giving the true anomaly in $[0, 2\pi]$. In addition, to see how much of the error would be in-plane, a way to compare the error from the true anomaly is needed. If all of the error were from true anomaly, as diagrammed by Fig. 25, the positional error would be

$$e = 2R \sin \frac{\Delta\nu}{2}. \tag{32}$$

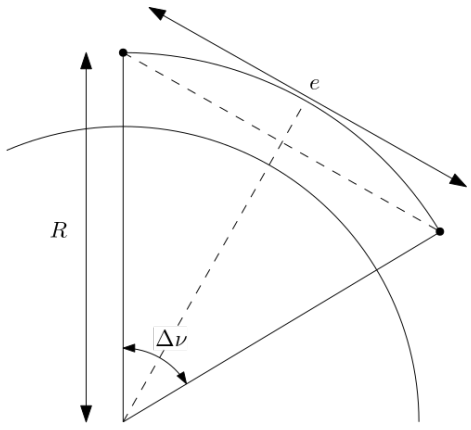

Figure 25. True anomaly error to positional error.

However, since the positional error is measured in fractions of the xGEO orbit

radius, the equivalent error would also be in terms of the orbit radius,

$$\tilde{e} = 2 \sin \frac{\Delta\nu}{2}. \tag{33}$$

Notice that for small $\Delta\nu$ that the fractional error is simply the angular error in radians, assuming a small angle approximation, so that they can be directly compared.

3.2 Observability

To test how well xGEO orbits can be used to perform cislunar SDA, STK is used to create constellations at 1-4xGEO and simulated sensor performance against a lunar mission test satellite. First, the models of the constellation, sensor design, exposure time, and test trajectory are explained. Then, the metric created to compare the observation results is discussed.

3.2.1 Models.

First, a lunar mission test satellite is chosen since it represents one of the hardest cislunar missions to observe due to the large ranges, and is similar to Bolden's work [3]. This test orbit does not contain the orbit from the Moon back to Earth. It is created using Astrogator's mission planning tool, launching from an initial condition of a LEO orbit in the lunar plane, then a maneuver to move towards the moon and captured by the lunar gravity to be pulled into a lunar orbit. Visualized in Fig. 26, the red line represents the first part of the trajectory while it's targeting the Moon, while the yellow line represents the maneuver to launch into a lunar orbit. This is limited to a single plane by creating the initial conditions of a lunar plane LEO orbit and only allowing maneuvers in the lunar plane. This is done to minimize computation time and analytical complexity.

Once a test orbit is decided, the observing constellations need to be designed.

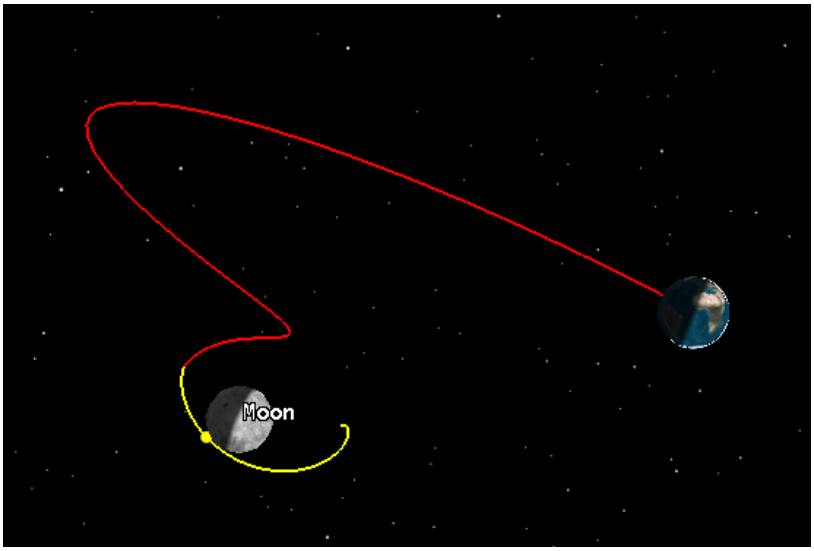

Figure 26. Lunar test orbit simulated by STK.

Similar to the test orbit, to reduce analytical complexity, the observation orbits are limited to the lunar plane at that particular radius (1-4xGEO). The number of satellites in each orbit also have to increase for larger orbits, since as the radius expands, the circumference expands by the same factor, and the observable sphere expands as a cubic. The number of satellites in the single orbit should increase by the radius to account for the increased distance between its neighboring satellites. This can be seen when derived by equating the distances of two constellations, one at GEO and another at some multiple of GEO,

$$d_{\text{GEO}} = d_{\text{xGEO}} \tag{34}$$

$$2r_{\text{GEO}} \sin\frac{\theta_{\text{GEO}}}{2} = 2xr_{\text{GEO}} \sin\frac{\theta_{\text{xGEO}}}{2} \tag{35}$$

$$r_{\text{GEO}}\theta_{\text{GEO}} \approx 2xr_{\text{GEO}}\theta_{\text{xGEO}} \tag{36}$$

$$\theta_{\text{xGEO}} \approx \frac{1}{x}\theta_{\text{GEO}} \tag{37}$$

given the small angle approximation and where d represents the distance between satellites, $r_{\text{GEO}} = 42164$ km, and $x = 2, 3, 4$ for multiples of GEO. As an arbitrary

starting number, twenty four satellites were put in the 1xGEO constellation, meaning a satellite every fifteen degrees. To make a 2xGEO constellation have the same distance between satellites, the arclength shortens to 7.5 degrees per satellite, decreasing by a factor of 2. The total number of satellites in each orbit can be seen in Table 2.

Table 2. Satellites in each xGEO orbit radius.

xGEO Radius	Number of Satellites	Deg per Satellite
1	24	15
2	48	7.5
3	72	5
4	96	3.75

The sensor is designed to function like the Sapphire satellite from Canada [12]. Specifically, the sensor has an aperture diameter of 15 cm and a focal length of 60 cm. The FOV is the same as Sapphire at 1.4 deg by 1.4 deg, and with 1024 x 1024 pixels. The exposure time is set at 1 s, with integration timesteps every 60 seconds. There is an argument to be made that just as the number of satellite in each xGEO orbit should increase, the sensor design, exposure time, and other CONOPs decisions should scale according to orbit radius as well. However, since this research effort is only interested in the performance of the orbits themselves, this is not done.

The STK EOIR module calculates SNR through careful simulation of the universe, called a "Modeled Universe of Interest", or an MUI [13]. It consists of "the Sun, the planets in the Solar System, the Moon, and a star field", as well as a limited number of user inputted objects. With a maximum of 16 observation satellites, a synthetic scene is simulated and generated, outputting a "two-dimensional array of spectral radiance vectors" [13]. If sensor saturation is neglected, the SNR is then calculated

using this equation,

$$\text{SNR} = \left| E^{\text{tgt}} - L^{\text{bkg}} \Omega_T \right| \frac{\mathfrak{R}_{\text{peak,E}}}{\sigma}, \tag{38}$$

where

- E^{tgt} = the target spectral irradiance at the sensor aperture
- L^{bkg} = uniform apparent background spectral radiance at the sensor aperture from the area behind the target
- $\Omega_T = A/R^2$ = the solid angle subtended by the target, or the projected area of the target divided by its distance squared
- $\mathfrak{R}_{\text{peak,E}}$ = the peak radiance responsitivity, measured in [electrons/(W/(cm^2 sr))]
- $\sigma = \sqrt{ne^2_{\text{dark}} + ne^2_{\text{photon}}(L_{\text{B,eff}})}$ = the root mean square deviations in sensor response [electrons] for the local IFOVs surrounding the target-containing IFOV.

3.2.2 Metrics.

Two general factors in any SDA mission is the quality of the observation and how long the object is in view. Since the EOIR module provides the simulated SNR, the total time target object is observable can be found by assuming any observation with a SNR of 6 or higher is successful, as it is often considered the minimum SNR needed [14, 15]. Therefore, given that the SNR and time observable are the two metrics of interest, we can combine the two by using SNR hours, an equal combination of length of successful observations and higher SNRs for better observations. This is calculated by summing up each timestep,

$$\text{SNR hrs} = \sum_{i}^{N} \text{SNR}_i \Delta t_i \tag{39}$$

where SNR_i is the ith timestep's measured SNR, Δt_i is the length of that particular timestep in hours, and N is the total number of timesteps.

Seeing how the observation satellite moves with respect to the target is also important. For that reason, two other metrics were plotted along with the SNR, the range to target and the sun angle. Both are given by STK, but STK gives the sun angle in terms of the Sun-observation-target, as shown below in Fig. 27. In other words, if the sensor is pointing nadir and the Sun is located at zenith, the sun angle would be 180 degrees.

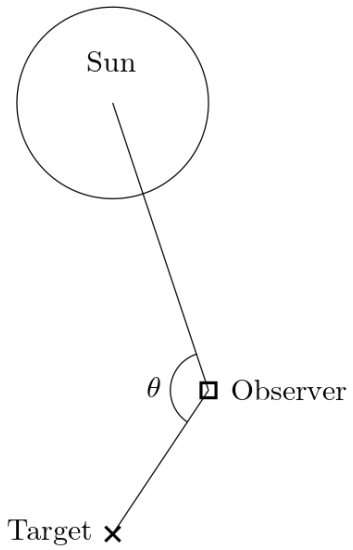

Figure 27. STK-defined Sun Angle

3.3 Lagrange Point Inspection Mission

The last objective is finding the feasibility of using these xGEO orbits to inject into an orbit around L_1. This can be used for many different missions, such as an inspection mission for an L_1 satellite, or even an on-orbit-servicing mission. In the two dimensional case, the stable manifold from L_1 Lyapunov orbits do not intersect with GEO orbits, but they do intersect with 2xGEO orbits and higher, meaning that guesses for minimum Δv transfers can easily be found. This can be seen in Fig. 28,

where the smallest green circle represents 1xGEO, and each increasing green circle are integer multiples of GEO.

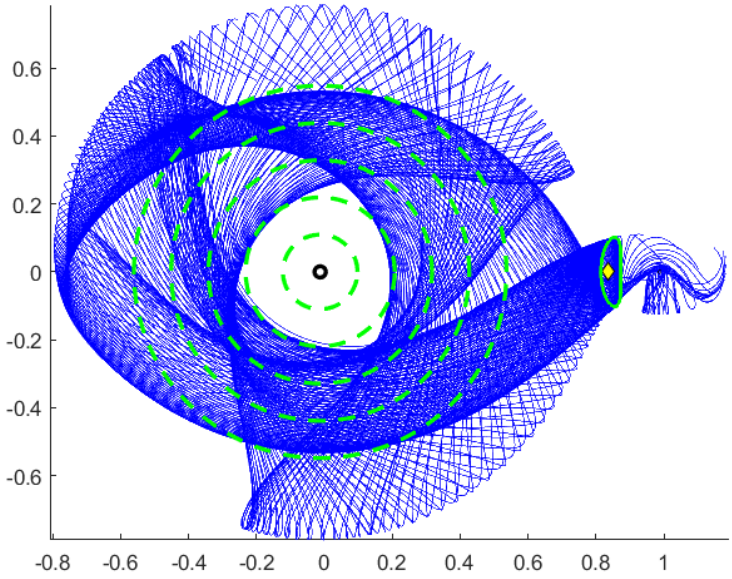

Figure 28. Stable manifold connecting with 2xGEO and higher orbits.

The CR3BP is simulated and the connection points for minimum time and minimum Δv were found with MATLAB to show that the trajectory is possible. These can eventually be used as initial guesses in some full-body integrator like Astrogator to differentially correct and control to an orbit around L_1.

3.3.1 Models.

The way to create the initial guesses is by using the stable manifolds of L_1. As discussed in Section 2.4, the manifolds are created from the eigenvectors of the monodromy matrix from a periodic orbit. In this case, a Lyapunov orbit around L_1 is created using a differential correction scheme, using steps in the x direction with magnitude A_ξ, as discussed in Section 2.3.3, using the CR3BP equations of motion. The results of this process can be seen in Fig. 29.

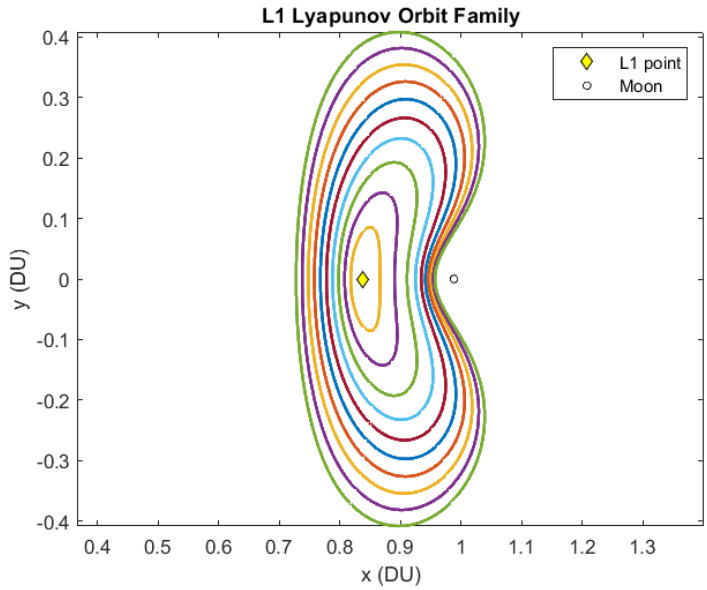

Figure 29. Lyapunov orbit family.

Larger Lyapunov orbits would require less Δv and less time, thus a worse way to compare orbits. However, Lyapunov orbits too small create manifolds that integrate towards the Moon, as shown in Fig. 30.

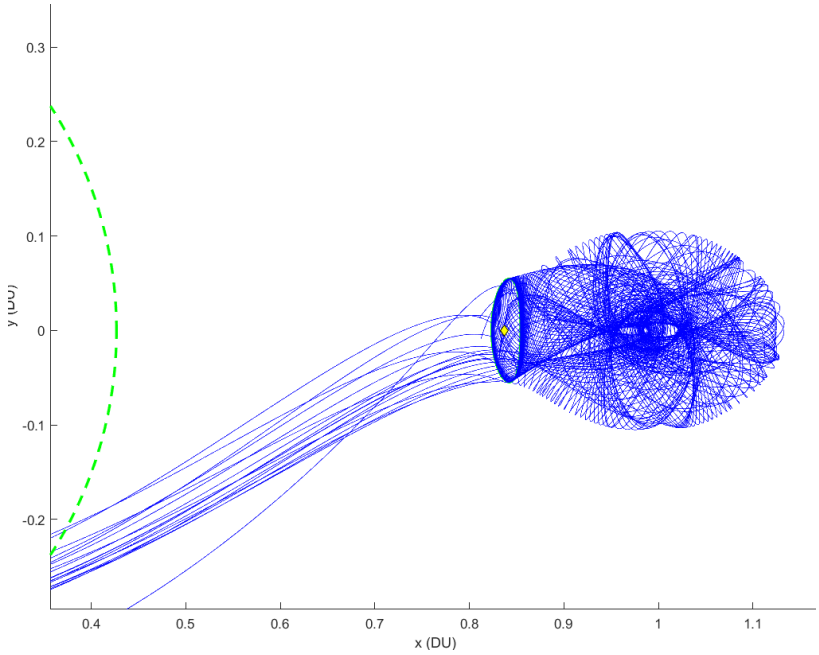

Figure 30. The manifold of a $A_\xi = 5200$ km Lyapunov orbit.

Ultimately, a Lyapunov orbit of $A_\xi = 9044$ km is chosen for nicely behaved manifolds that lead towards Earth. Starting from 5200 km, and steps of 384.4 m, the tenth Lyapunov orbit generated is chosen as the target Lyapunov orbit. The manifolds were then created by perturbing the position and velocity states of the Lyapunov orbit by the eigenvectors of the monodromy matrix. Since the stable manifolds integrate towards the Lyapunov orbit, the perturbation is then integrated backwards in time, in this case, over two lunar periods (4π in unitless time). Once the manifolds have been created using this process, the bifurcations of xGEO orbits can then be found by calculating the distance from Earth center of every point in the manifold. Since everything is in the barycentric frame, this can be accomplished by adding μ in the x direction and then taking the norm of that vector. In other words, checking for

$$\text{abs}\left(\text{norm}(\vec{r} + \mu\hat{x}) - r_{GEO}\right) \leq \epsilon$$

where $\vec{r}$ is a point in the manifold, μ is the mass parameter, r_{GEO} is 42,164 km and the geosynchronous radius, and ϵ is some small non-zero number. ϵ cannot be zero since the manifolds are not continuous, and are discrete points decided by the integrating function generating the manifolds. This can be seen in Fig. 31, where the red circles represent the discrete points on the manifold, and the green dashed line is the circular 4xGEO orbit.

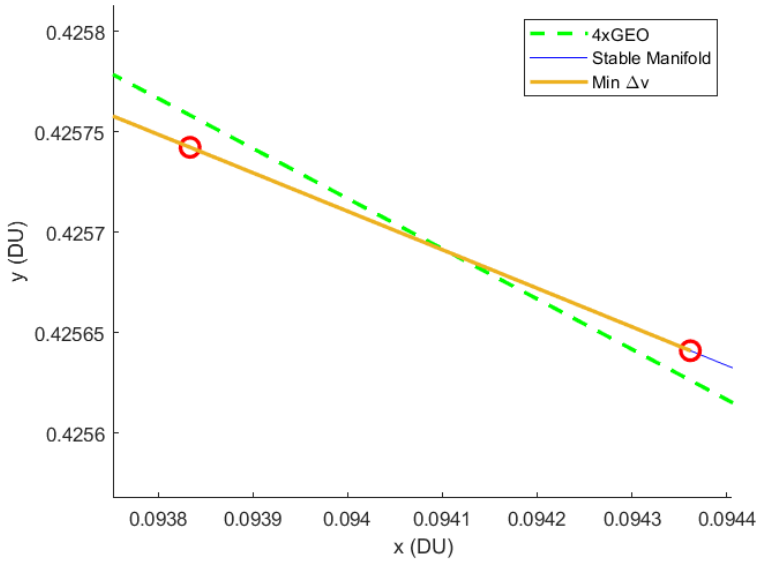

Figure 31. Error due to discretization of manifolds.

Using `ode45` with a relative tolerance of 10^{-13} and an absolute tolerance of 10^{-15}, an epsilon of 10^{-5} is used, which corresponds to a sensitivity of 4 km. This is .009% the distance of geosynchronous orbit, and considered negligible, especially since the manifolds are already confirmed to intersect with xGEO orbits.

3.3.2 Metrics.

The two metrics of interest for this objective are the time of flight and total Δv. The sources of Δv are taken from the Δv needed to eject from the xGEO orbit onto the manifold, then from the manifold to the Lyapunov orbit. Due to the small perturbation off the Lyapunov orbit, the second Δv is usually on the scale of 10^{-6}. The time of flight is measured from the first Δv to when the satellite reaches the Lyapunov orbit. Since these two metrics are generally inversely related (a longer time of flight will allow for better Δv solutions), two solutions were generated for each xGEO orbit— one for the smallest Δv and another for the shortest amount of time.

3.4 Summary

This chapter explained the tools used to perform the three research objectives outlined in Chapter I. First, MATLAB is used to compare three different models of orbital trajectories, where errors were measured as fractions of the orbital radius. STK is used to create the full-body Ephemeris trajectory, while the two-body and circular restricted three body models were created in MATLAB. Secondly, a lunar satellite trajectory created through STK is used as a test observation target at different xGEO orbits. Using a metric of SNR-hours is an easily measured way to measure feasibility. Lastly, MATLAB is used to find intersections of the xGEO in the lunar plane and the stable manifold of an L1 Lyapunov orbit. Next, the results of the metrics developed in the chapter will be presented and analyzed.

IV. Analysis

This chapter reports on the metrics of interest in the three objectives as described in Chapter III. Overall, most of the error was in-plane, the xGEO orbit observational satellites performed well compared to a GEO constellation, and minimum Δv trajectories were successfully found between xGEO orbits and a L_1 Lyapunov orbit.

4.1 Orbit Analysis

First, a graph of the orbits themselves is presented in Fig. 32. Blue represents the two body assumption of only the Earth as a gravitational source, orange represents the circular restricted three body assumption, while the yellow represents the full body Ephemeris model from STK.

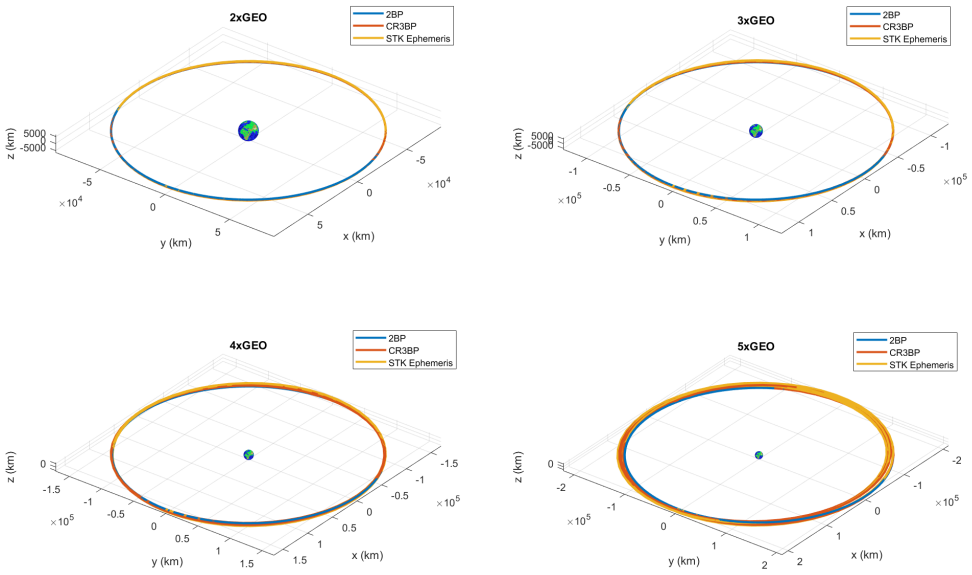

Figure 32. 2xGEO through 5xGEO orbits with three different models.

From left to right, top to bottom, the 2-5xGEO orbits are graphed, and it can be seen graphically that the further away from the Earth the orbits are results in

higher error. This can be seen in the errors as a fraction of xGEO radius in Fig. 33, calculated as

$$\tilde{e}_i = \frac{\vec{r}_{\mathrm{i}} - \vec{r}_{\mathrm{Ephemeris}}}{R},$$

where i can represent either the two-body or three-body models and R is the orbit radius.

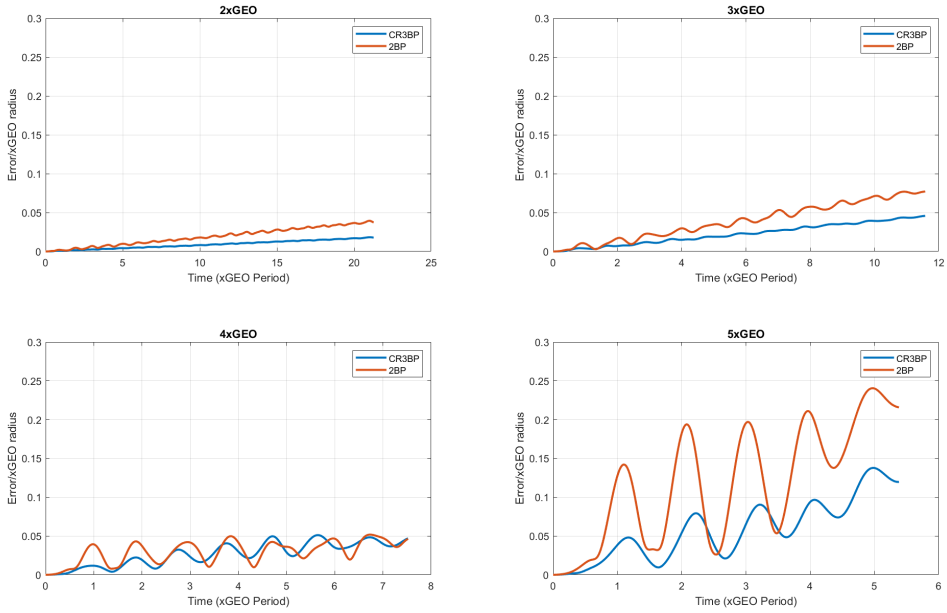

Figure 33. Positional error over the orbits' period.

As mentioned in Section 3.1.2, the errors grew roughly proportional to the radius and can be seen in the figure, since they exist on the same scale when normalized by the orbit radius. The only exception seems to be 5xGEO, where the errors are 25% of the radius. This is most likely due to the nonlinear effects of all the other third body perturbations on the Ephemeris model, and increasing the error of both the 2BP and CR3BP models. All errors have an oscillatory behavior with a period approximately equal to the orbit period, but vary by a small amount depending on the radius.

As seen in Fig. 34, oscillations in the errors can be explained as the Ephemeris

model experiencing an increase in true anomaly for half the period, and then a decrease in the second half of the period, as generally the third body perturbations stay in roughly the same direction during the orbital period. If done over a longer period of time, one would expect a phase change corresponding to the changing direction of perturbations (the Sun and Jupiter changing directions in the ICRF).

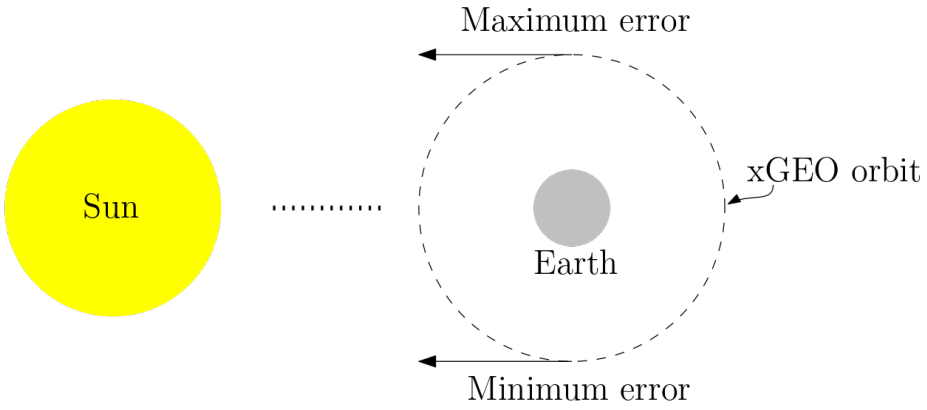

Figure 34. Third body perturbation of the Sun.

To find out how much of that error is in plane, the instantaneous "true anomaly" is examined, as described in Section 3.1. First examining Fig. 35, which graphs the true anomaly difference, it is clear that higher orbits mean larger relative phase changes. In fact, when compared to Fig. 33, the in-plane error is the leading source of error, as they match very closely.

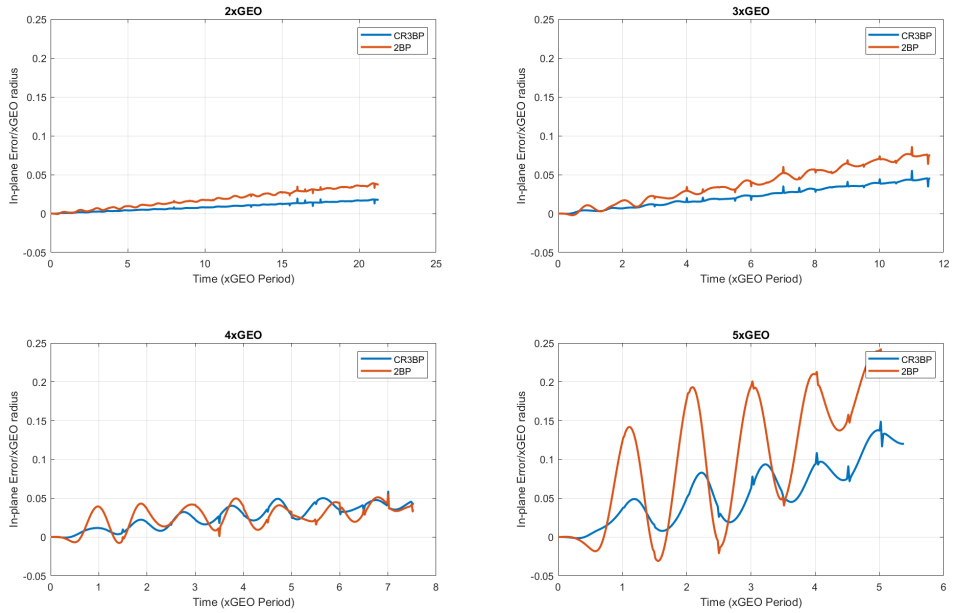

Figure 35. Normalized error from the in-plane true anomaly difference.

There is a spiking behavior that only exists in Fig. 35, which happens every half period, most of which are too small to be seen. There is a small phase shift that increases with orbit radius such that the spikes are not exactly at half periods, but are often on the order of .01 xGEO periods. One way to explore why this may be happening is examining the true anomaly rate. As seen in Fig. 36, the true anomaly rate is also periodic, suggesting that there is some acceleration approximately constant in direction speeding it up for half the orbit and slowing it down for the other half. The oscillation of the true anomaly rate also proves that these orbits are non circular, compared to the constant rate of the 2BP model shown in orange.

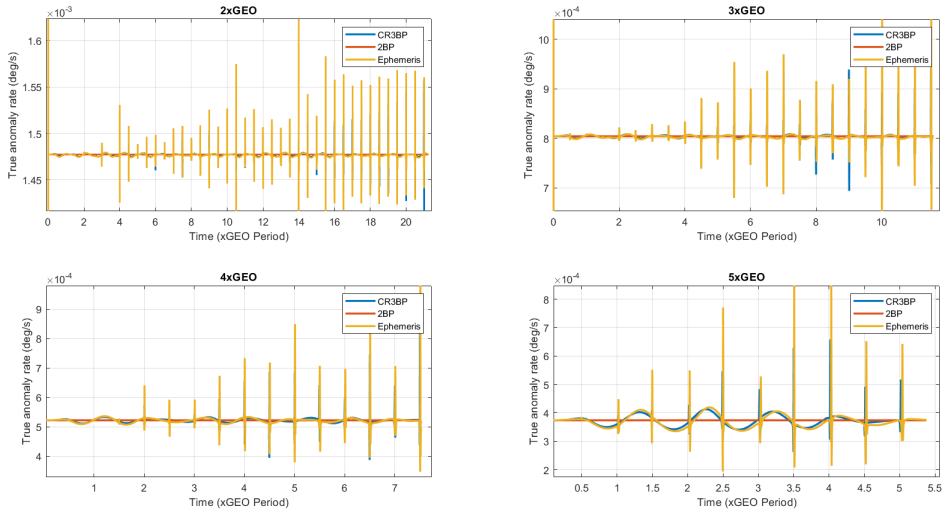

Figure 36. True anomaly rate of each model.

The true anomaly rate also exhibits the spiking behavior at every half period, which when magnified, has a decrease in true anomaly rate before spiking, then returning to its "original" position, as shown by Fig. 37. Such a spike in true anomaly rate may be caused by out of plane motion; since the true anomaly is calculated as the angle between the initial position vector and the current position vector, any acceleration away from the orbit plane would be an increase in the true anomaly rate, and vice versa.

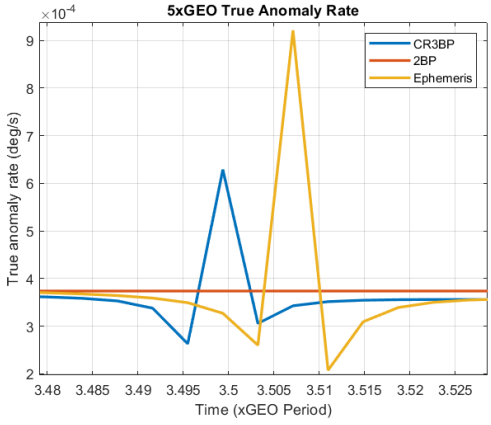

Figure 37. True anomaly rate of 5xGEO magnified.

Therefore, since the z motion (away from the orbit plane) is periodic, as seen in Fig. 38, this would result in the spiking motion seen in Fig. 35 and Fig. 36 whenever the z is minimum or maximum.

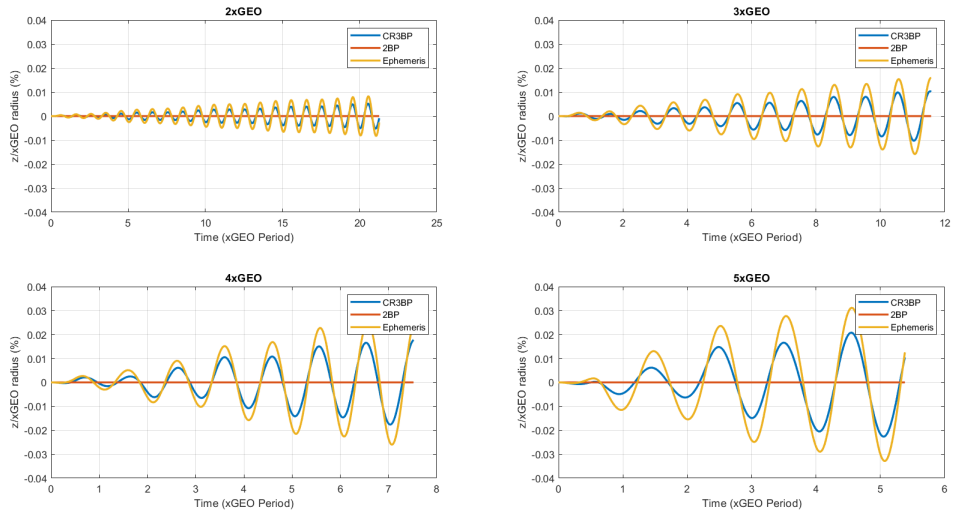

Figure 38. Z-axis contributions to error.

4.2 Observability

Next, the results of the second research objective, finding how well these orbits can be used to perform space-based SDA, are discussed. First, the overall results will be discussed, then individual discussion of each satellite constellation are discussed.

The results of the constellations can be seen in Fig. 39 and 40. The graph on the top represents the simulated SNR given by STK calculations described in Section 3.2, where the satellite with the highest SNR is selected and plotted. For the most part, the relative speeds of the test satellite and the observation satellites were such that the custody did not matter and only one satellite had custody the entire time. In addition, the chosen integration value of 1 second caused SNR values that saturated every sensor, especially the 2-5xGEO constellations. This reflects the need for either different sensors or different CONOPs/integration times depending on the orbit it

was meant for.

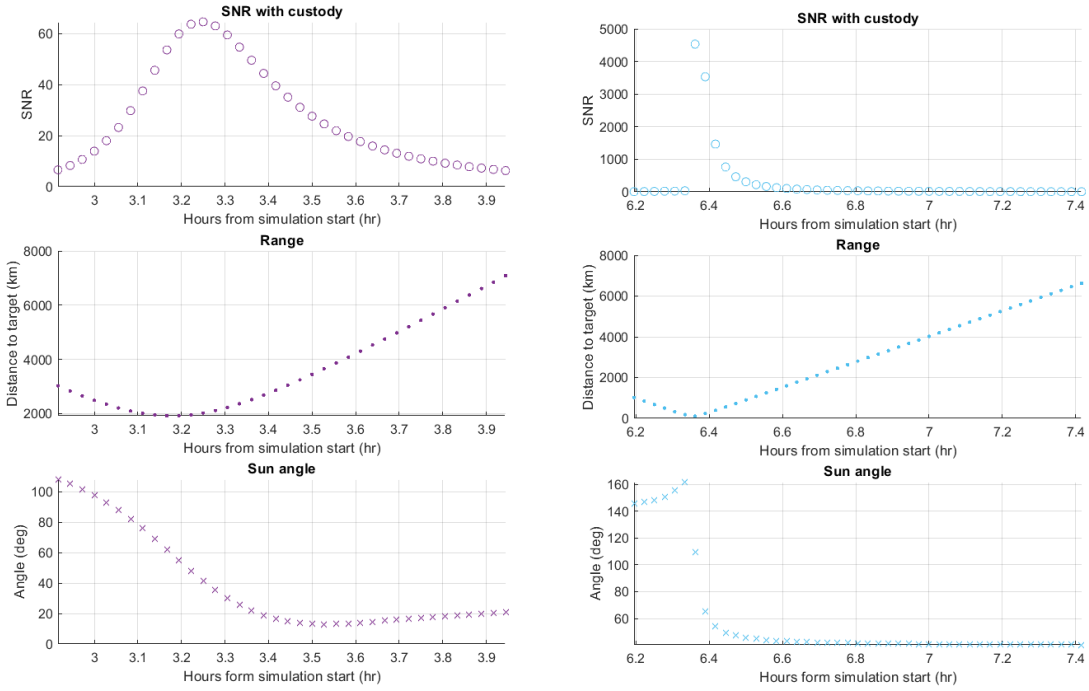

(a) 1xGEO.

(b) 2xGEO.

Figure 39. 1 and 2xGEO observation results without accounting for saturation.

To account of the saturation of sensors, an SNR saturation limit was decided at three times the minimum, at an SNR of 18. This means that any observation with an SNR of above 18 will be discounted, and the satellite with the next best SNR under 18 will be used.

The range and sun angle were also plotted to help interpret the data, where the sun angle is defined as the Sun-observer-target angle. Generally, the closer the range is to zero and sun angle to 180, the better the SNR will be. However, as seen in Fig. 39, the way the target is moving from the Earth to Moon, when the target reaches minimum range the sun angle is still between 60-100 degrees, so the peak SNR happens between the minimum range and best sun angle.

Another relationship of interest is between the minimum range and the rate of

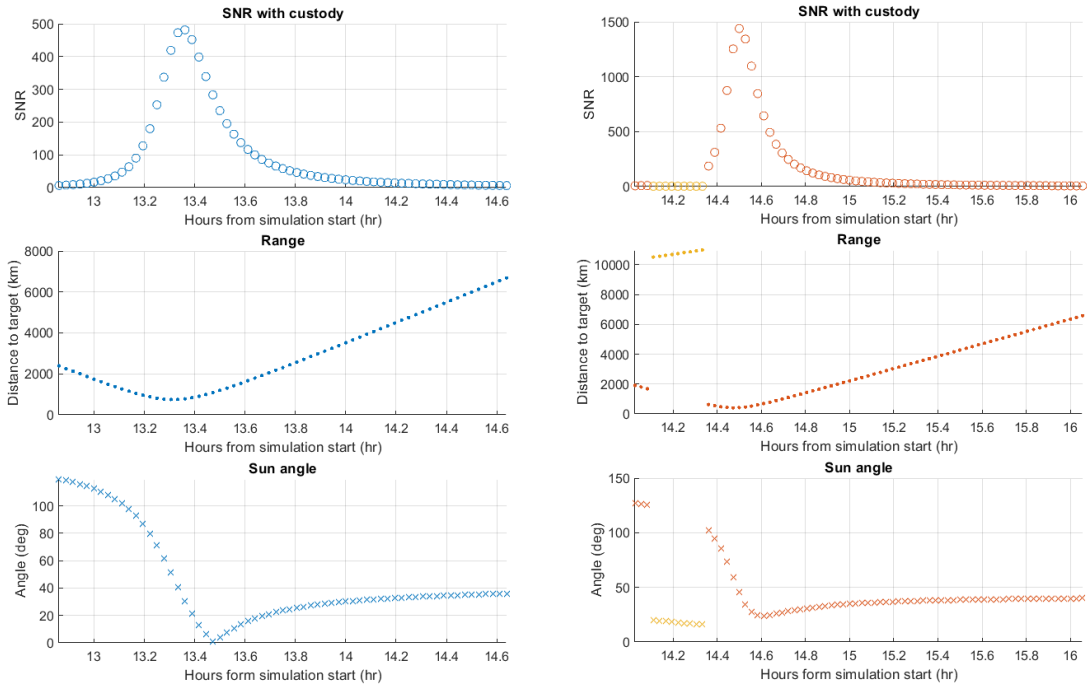

(a) 3xGEO.

(b) 4xGEO.

Figure 40. 3 and 4xGEO observation results without accounting for saturation.

change of the sun angle. In this simulation, it was assumed that the observation satellite can follow the target exactly, and therefore in Fig. 39b for the 2xGEO constellation, although the maximum SNR is very large due to the minimum range of 112 km, the angular rate at 6.3 hrs is 0.48 deg/s. Meanwhile the 1xGEO constellation has a much lower angular rate of 0.06 deg/sec with a minimum range of 1920 km. All slew rates were within the range of most satellites' capabilities, as well as Sapphire's capability [12, 16].

Fig. 40 show approximately the same results. They have the same relationships between range and sun angle, as well as range and sun angle's relationship with SNR. Similar to the 1xGEO constellation, the 3xGEO constellation also does not get as close as the others to the target, and its effects can be seen in the slew rate and the maximum SNR. The 4xGEO constellation has a 10 minute period of time where the

satellite with maximum SNR violated a pointing constraint, so another satellite had to take custody, as shown by the yellow data points.

Summing up the results for this section, Table 3 contains the final results in both observation time and total SNR hrs for each constellation. As expected, the observation time of each satellite constellation increased as the radius increased, due to the smaller angular velocity of larger orbits. Without the saturation CONOPs of switching to another satellite with lower SNR, the score for the 3-4xGEO constellations were actually lower than 2xGEO due to the variations in relative distance. As seen in the table, the enforcement of the saturation condition lessened the effect.

Table 3. Observation results.

Orbit	Observation Time (hr)	Score (SNR hr)
1xGEO	0.300	3.284
2xGEO	0.333	3.502
3xGEO	0.433	4.584
4xGEO	0.450	4.630

In conclusion, there is an improvement over purely GEO orbits just from the fact that the observation times are much larger, so that even if the minimum ranges were the same and had similar maximum SNRs, the scores of the larger orbits would be much higher.

4.3 Lagrange Point Inspection Mission

Lastly, the results of the third research objective are discussed. Since the manifolds do not intersect with any 1xGEO orbits, a maneuver is needed to reach the manifolds, while 2xGEO orbits and above directly intersected with these manifolds, such that only one instaneous Δv maneuver was needed to get on the stable manifold. Fig.

41 shows the minimum time and Δv solutions of trajectories from 2-5xGEO to a Lyapunov orbit around L_1.

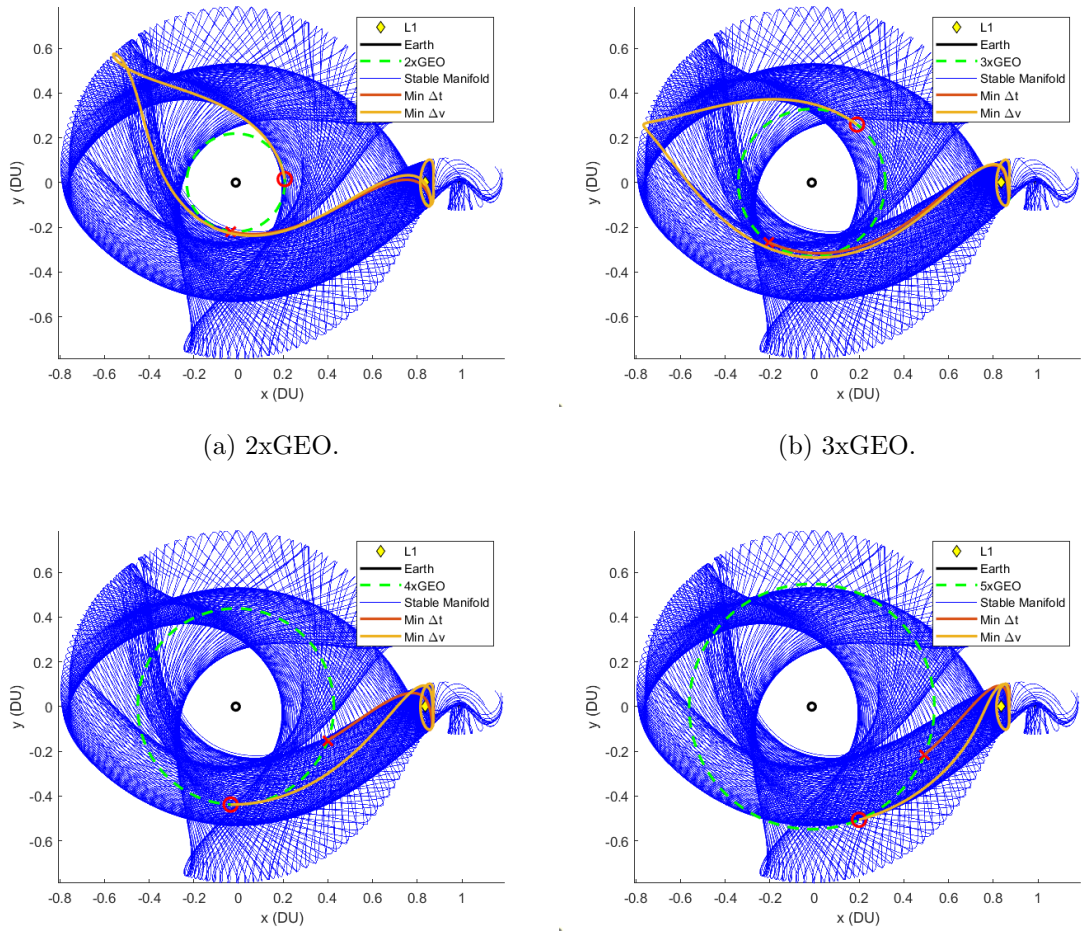

(a) 2xGEO.

(b) 3xGEO.

(c) 4xGEO.

(d) 5xGEO.

Figure 41. 2-5xGEO inspection mission solutions.

As shown in Fig. 41b and 41d, in some cases the minimum Δt will not be at the intersection point closest to the Lyapunov orbit, since the manifold may have some travel time near the Lyapunov orbit before actually reaching it. For example, for the 2xGEO to L_1 minimum time trajectory shown in Fig. 42, the trajectory follows the manifold around but not to the Lyapunov orbit until it reaches all the way around to the bottom.

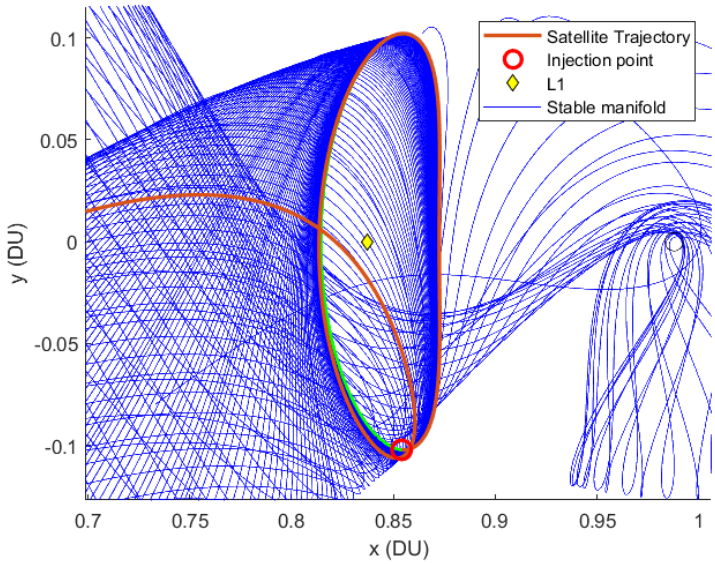

Figure 42. 2xGEO to L_1 trajectory.

As the radius increases bringing the xGEO orbit closer to the Moon, both the Δv and time of flight Δt were expected to decrease. However, as seen in Table 4, the Δt of the minimum time results stayed approximately the same (20-22 days) regardless of orbit above 2xGEO. This is due to the stable manifolds staying together shortly after leaving the Lyapunov orbit, leading to very similar solutions for minimum time regardless of the orbit radius.

The minimum Δv solutions are also grouped together in terms of Δt, with 2-3xGEO at 33 days and 4-5 xGEO together at 22.3-22.4 days. At 3xGEO and below, the stable manifold intersection with the xGEO orbit is at an angle such that 112 m/s and 169 m/s could be saved at a delay of 12 days, respectively. However, the Δv savings for larger orbits are much larger, presumably since the higher orbit already has more mechanical energy. With only a difference of two days, 4xGEO and 5xGEO orbits are able to save 602 m/s and 264 m/s of Δv respectively.

Table 4. 2-5xGEO inspection mission results

Orbit	Solution	ToF (days)	Delta v (m/s)
2xGEO	Min t	21.21	642
	Min v	33.21	530
3xGEO	Min t	21.72	479
	Min v	33.20	310
4xGEO	Min t	19.88	812
	Min v	22.31	210
5xGEO	Min t	20.00	404
	Min v	22.42	140

These results suggest that larger orbits, while allowing for smaller Δv and Δt, eventually have diminishing returns somewhere between 3-4xGEO. Combined with the increased Δv needed to get into these higher orbits compared to low orbits like LEO or GEO, these orbits may be useful only for certain applications.

4.4 Summary

This chapter presented the results of the study and explored the possible implications of the data. First, the orbit analysis data showed that the 2-5xGEO orbits are well defined as slightly perturbed two-body orbits, and in some cases, that the two-body model is even more accurate than the CR3BP model. Most of the orbit error from these models and the Ephemeris full body model are in-plane, and do not represent a fundamental change in any SDA CONOPs models. Next, the observability data showed that in general, the higher orbit geometry and better viewing angles gave higher SNR hours than the 1xGEO orbit constellation, although more cases and data are needed to fully confirm these findings. Lastly, the research showed that

higher xGEO orbits do take less time and Δv to maneuver to a L_1 Lyapunov orbit, but gives diminishing returns on the Δt and Δv savings between 3 and 4xGEO.

V. Conclusion

This study explores the possible untapped potential of xGEO orbits for cislunar SDA. One of the disadvantages of using cislunar orbits for cislunar SDA is the unpredictability of the orbits. If xGEO orbits can produce results showing SDA capability while having more predictable motion, then it may serve as a useful orbit blending the advantages of Earth bound orbits and cislunar orbits.

First, an orbital analysis of 2-5xGEO was done, and how closely the two-body and CR3BP models follow the Ephemeris model. In-plane motion accounted for greater than 98% of the errors, and had an increasing oscillatory motion over time. The error also increased proportionally with xGEO altitude, with the exception of 5xGEO where the error increased at a faster rate. The out-of-plane error in the z direction was also oscillatory and increasing in amplitude, but maintained a mean zero value.

Next an observational satellite constellation was created for 1-4xGEO and simulated observations of a test satellite going from LEO to an orbit around the Moon. While there were some problems with sensor saturation and variations in sensor-target distances, overall the results were promising. As expected with the higher orbits, the observation times were longer, even if the distances to the target were larger. This trade off is due to the high relative velocity but low relative angular velocity, since the target was moving roughly perpendicular to the observation satellite's trajectory. Although not explored in this study, in general for cislunar SDA architectures, satellites with closer range to target and greater geometric diversity will create better observations [3]. The application of these findings are to introduce these orbits into SDA architecture studies, where larger orbits may give better observations but with the trade-off of being harder to track or perhaps using more Δv to maintain that orbit.

The last research objective was finding ways to use these xGEO orbits to create a trajectory to an L_1 Lyapunov orbit. All orbits from 2-5xGEO did intersect with the stable manifolds to create valid trajectories within the CR3BP model. Although a full body Ephemeris model was not used, these can be used as first guesses and reliable indicators of what those results would behave like. As discussed in section 4.3, there are opportunities for trajectories with smaller Δv and Δt, but at some point there are diminishing returns between 3-4xGEO. One possible practical application of these findings may be to do on-orbit-servicing, where satellites can refuel at a refueling station around L_1, or perhaps to perform an inspection mission of a certain satellite that is more visible in L_1.

5.1 Future Work

There is a lot of work that can be done as a follow-on for this topic. For the orbit analysis portion of the work, a question of interest is how to maintain these orbits, or if it is even necessary to. First, if a satellite were to maneuver to maintain an xGEO orbit, how much Δv would it need to maintain that orbit? In addition, are there any minimum Δv orbits that are possibly non-circular? This second part will have a differential correction algorithm similar to how the Lyapunov orbits are created.

The second objective also has a lot of potential for follow-on work. The biggest limitation to the current study is the variation in the sensor to target distance. Some constellations had satellites much closer to the target than others. Future work could create multiple constellations with different true anomaly initial conditions to simulate and average the results together, creating a more objective way to compare the performance of these orbits. In addition to more cases, exploring the different sensor design and CONOPs of the observation satellites may also prove to be useful. The unrealistic assumption that the satellite can always rotate such that it's pointing at

the target resulting in angular velocities of 33 deg/s also leads to higher than normal SNR values. The effect is mitigated by setting an SNR saturation point such that the high angular velocity values are never reached, but enforcing this constraint in the simulation itself would be more realistic.

The last objective, creating a trajectory from xGEO to a L_1 Lyapunov orbit, also has great opportunities to explore. The biggest limitation to the current study is that it only uses the CR3BP as the model. Using a higher fidelity model with a differential corrector or optimal control would provide more accurate and relevant results. The results of this study would serve well as initial guesses for this future work. In addition, this study of an xGEO-L_1 trajectory only considered up to the Lyapunov orbit and never explored the control needed to maintain that orbit. Such an application of controls would be needed for a satellite to accurately perform the mission.

5.2 Summary

Given the results and analysis of xGEO orbits, further research is needed for more accuracy and with higher fidelity. This study lays a foundation and provides initial results for future work into xGEO orbits and their uses. However, existing results already present an attractive orbit to use for a number of purposes for cislunar missions, including SDA, inspection, or on-orbit-servicing.

Appendix A. Constants

These are all constants used in the MATLAB data analysis. r_{L_1} is the value given in the x direction, and A_ξ is the initial step in the x direction to create the Lyapunov orbit.

Table 5. Constants used.

Constant	Value
μ_{Sun}	132712440040.944 km^3/s^2
μ_{Earth}	398600.436233 km^3/s^2
μ_{Moon}	4902.800076 km^3/s^2
r_{12}	384400 km
r_{GEO}	42164 km
r_{L_1}	0.83692 DU
A_ξ	5200 km

Appendix B. Extra Data

For the orbit analysis, the instantaneous true anomaly of each orbit given the same initial condition is graphed here in Fig. 43.

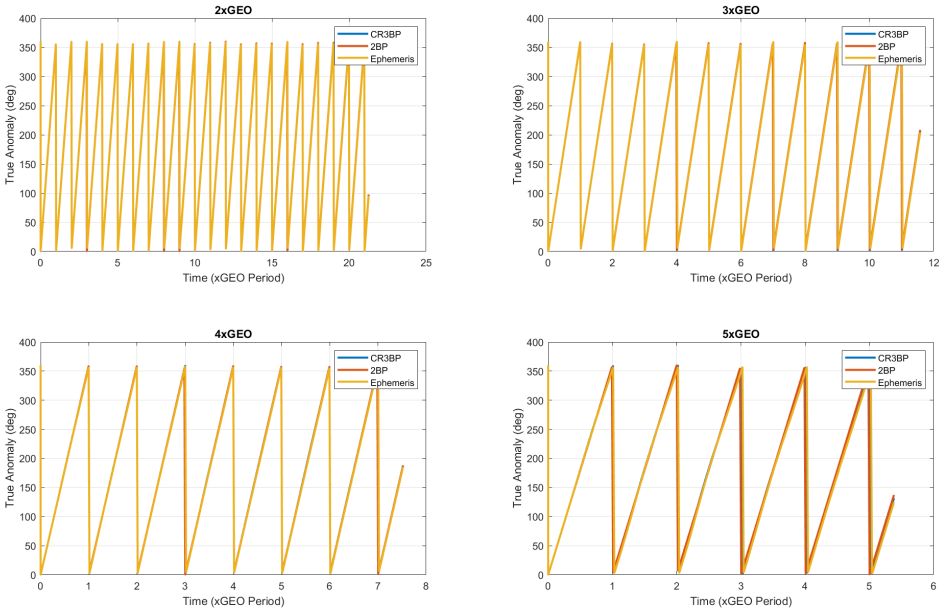

Figure 43. The instantaneous true anomaly of each orbit.

There was also some differences in where orbits transitioned from 360 degrees to 0 due to discrete timesteps. In 2-4xGEO, all models change at the same timestep, but at 5xGEO the 2BP model was too far ahead of the other models and wrapped to zero beforehand.

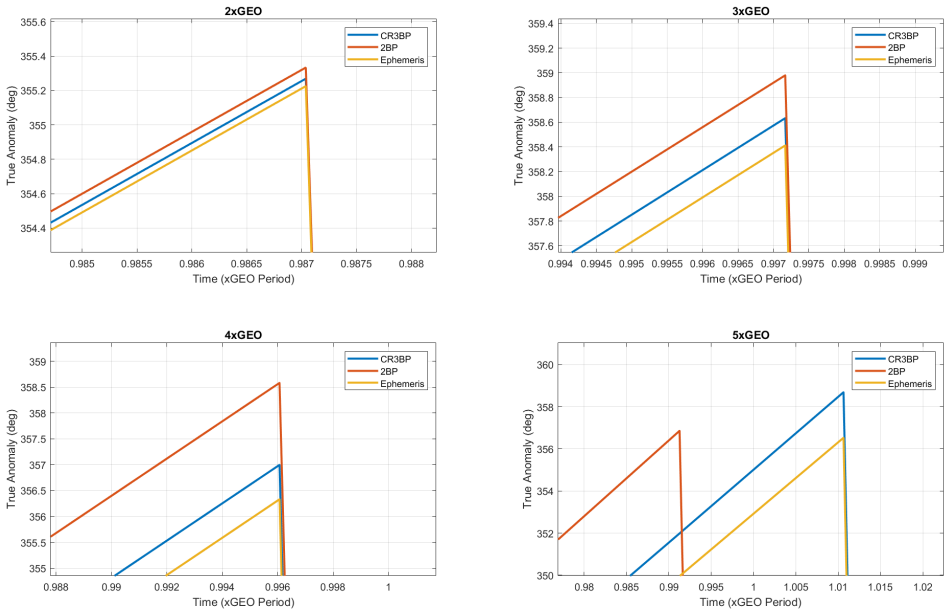

Figure 44. True anomaly during the first period.

Including the Sun into the CR3BP, understandably, also makes the errors go down. It is interesting to note that at 3xGEO, even with the Sun as an extra perturbation, results in a higher normalized error compared to 4 and 5xGEO, which was not seen in the CR3BP model.

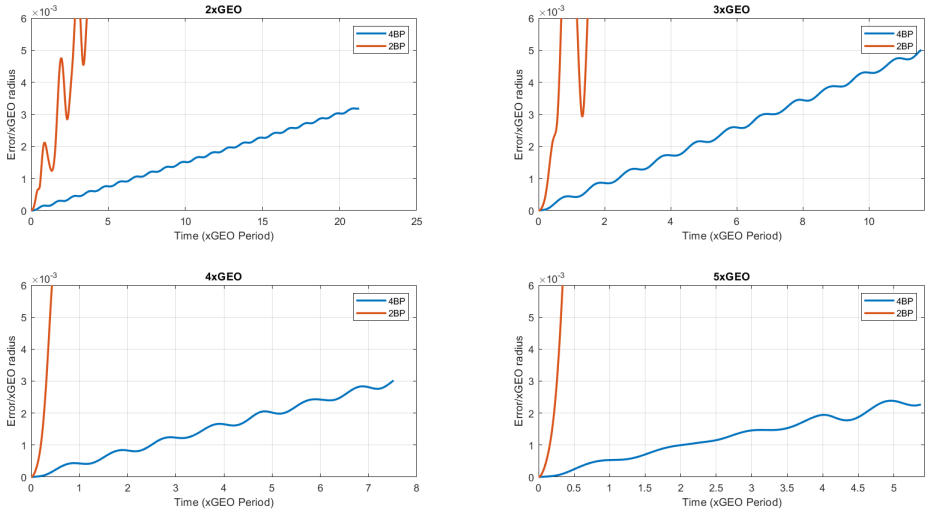

Figure 45. Position difference of 2BP and 4BP and Ephemeris model

Appendix C. Observation Specifications

Table 6. Sensor Specifications

Constant	Value
FOV	1.4 x 1.4 deg
Pixels	1024 x 1024 pixels
Spectral Band Edge Wavelengths	0.3-0.9 μm
F/#	4
Effective focal length	60 cm
Integration time	1 s

Table 7. Target Specifications

Constant	Value
Object	Grey body sphere
Reflectance	80%
Radius	1.5 m
Static Body Temperature	273 K

Bibliography

1. B. Chance Saltzman, B. A. D., "Memorandum of Understanding between the National Aeronautics and Space Administration and the United States Space Force," Tech. rep., USSF, NASA, Sept. 2020.

2. Holzinger, M., Chow, C., and Garretson, P., *A Primer on Cislunar Space*, Air Force Research Laboratory, 2021.

3. Bolden, M., Craychee, T., and Griggs, E., "An Evaluation of Observing Constellation Orbit Stability, Low Signal-to-Noise, and the Too-Short-Arc Challenges in the Cislunar Domain," *Advanced Maui Optical and Space Surveillance Technologies Conference (AMOS)*, 2020.

4. Fowler, E. E., Hurtt, S. B., and Paley, D. A., "Observability Metrics for Space-Based Cislunar Domain Awareness," *AAS/AIAA Astrodynamics Specialist Conference*, 2020.

5. York, C. E. and Howell, K. C., "A two-level differential corrections algorithm for low-thrust spacecraft trajectory targeting," *29th AAS/AIAA Space Flight Mechanics Meeting*, pp. 1–20.

6. Grebow, D., *Generating Periodic Orbits in the Circular Restricted Three-Body Problem With Applications To Lunar South Pole Coverage*, Master's thesis, Purdue University, 2006.

7. Zimovan, E. M., Howell, K. C., and Davis, D. C., "Near rectilinear halo orbits and their application in cislunar space," *Advances in the Astronautical Sciences*, Vol. 161, 2017.

8. Peng, H., Chen, B., and Wu, Z., "Multi-objective transfer to libration-point orbits via the mixed low-thrust and invariant-manifold approach," *Nonlinear Dynamics*, Vol. 77, 2014.

9. Gómez, G., Koon, W. S., Lo, M. W., Marsden, J. E., Masdemont, J., and Ross, S. D., "Connecting orbits and invariant manifolds in the spatial restricted three-body problem," *Nonlinearity*, Vol. 17, 2004.

10. Topputo, F., "Fast numerical approximation of invariant manifolds in the circular restricted three-body problem," *Communications in Nonlinear Science and Numerical Simulation*, Vol. 32, 2016.

11. Cox, A. D., Howell, K. C., and Folta, D. C., "Transit and capture in the planar three-body problem leveraging low-thrust invariant manifolds," *Celestial Mechanics and Dynamical Astronomy*, Vol. 133, 2021.

12. Hackett, J., Brisby, R., and Smith, K., "Overview of the Sapphire payload for space surveillance," *Sensors and Systems for Space Applications V*, Vol. 8385, International Society for Optics and Photonics, 2012, p. 83850W.

13. Space Dynamics Laboratory, 1695 North Research Park Way, North Logan, Utah, *STK EOIR Model Description and Validation*, December 2010, Available at *https://help.agi.com/stk/LinkedDocuments/EOIRModelDescriptionandValidation.pdf*.

14. Jaunzemis, A. D., Holzinger, M. J., and Jah, M. K., "Evidence-based sensor tasking for space domain awareness," *Advanced Maui Optical and Space Surveillance Technologies Conference*, Maui Economic Development Board Maui, HI, 2016, p. 33.

15. Silva, E., Van Cleve, J., Philbrick, R., Grant, C. J., Griesbach, J. D., and Mahoney, M. P., "System and Methods for Hybrid Lunar Surface and Space Domain Situational Awareness," *AMOS 2021*, 2021.

16. Votel, R. and Sinclair, D., "Comparison of control moment gyros and reaction wheels for small earth-observing satellites," 2012.

REPORT DOCUMENTATION PAGE

Form Approved
OMB No. 0704–0188

1. REPORT DATE *(DD–MM–YYYY)*	2. REPORT TYPE	3. DATES COVERED *(From — To)*
03-03-2022	Master's Thesis	Sept 2020 — Mar 2022

4. TITLE AND SUBTITLE

Leveraging xGEO Orbits for Cislunar SDA

5a. CONTRACT NUMBER

5b. GRANT NUMBER

5c. PROGRAM ELEMENT NUMBER

6. AUTHOR(S)

Jay Laone

5d. PROJECT NUMBER

5e. TASK NUMBER

5f. WORK UNIT NUMBER

7. PERFORMING ORGANIZATION NAME(S) AND ADDRESS(ES)

Air Force Institute of Technology
Graduate School of Engineering and Management (AFIT/EN)
2950 Hobson Way
WPAFB OH 45433-7765

8. PERFORMING ORGANIZATION REPORT NUMBER

AFIT-ENY-MS-22-M-302

9. SPONSORING / MONITORING AGENCY NAME(S) AND ADDRESS(ES)

10. SPONSOR/MONITOR'S ACRONYM(S)

11. SPONSOR/MONITOR'S REPORT NUMBER(S)

12. DISTRIBUTION / AVAILABILITY STATEMENT

DISTRIBUTION STATEMENT A:
APPROVED FOR PUBLIC RELEASE; DISTRIBUTION UNLIMITED.

13. SUPPLEMENTARY NOTES

14. ABSTRACT

With recent interest in using cislunar orbits for a variety of missions, it is more important than ever to also have cislunar space domain awareness. This thesis aims to bridge the gap between traditional LEO/GEO architectures and the new cislunar orbit architectures with orbits higher than GEO but still within the Earth sphere of influence, called xGEO. This research effort first explores the feasibility of xGEO orbits by examining the errors that the two-body assumption builds over time. Findings suggest that the two body assumption can be used to varying degrees depending on the orbit radius. This study has found that regardless of radius from 2-5xGEO, when the orbit is in the lunar plane, the majority of the error is in-track. The study then evaluates how well these orbits perform when observing a lunar mission test satellite. Lastly, this study explores the possibility of using xGEO orbits for an inspection mission at L_1.

15. SUBJECT TERMS

xGEO orbits,cislunar,CR3BP,inspection

16. SECURITY CLASSIFICATION OF:			17. LIMITATION OF ABSTRACT	18. NUMBER OF PAGES	19a. NAME OF RESPONSIBLE PERSON
a. REPORT	b. ABSTRACT	c. THIS PAGE			Lt Col Bryan Little, AFIT/ENY
U	U	U	U	84	19b. TELEPHONE NUMBER *(include area code)* (937) 255-3636, x4901; bryan.little@afit.edu